An Attempt to Synthesize Mn-doped Pyrite Thin Films

A THESIS

SUBMITTED TO THE FACULTY OF THE GRADUATE SCHOOL

OF THE UNIVERSITY OF MINNESOTA

BY

Yanjun Yang

IN PARTIAL FULFILLMENT OF THE REQUIREMENTS

FOR THE DEGREE OF

MASTER OF SCIENCE

Advisors: Chris Leighton

Eray S. Aydil

December, 2016

Acknowledgments

Above all, I would greatly thank my two advisors, Prof. Chris Leighton and Prof. Eray S. Aydil. I sincerely thank them for providing me the chance to work on this wonderful project, even though I only had a background in theoretical physics before joining this group. I thank them for motivating me, advising me, teaching me, and everything I learned in the group. I thank them for their generous support and all the help they have done for me.

I would like to thank Prof. Rafael Fernandes and Prof. James Kakalios for agreeing to be members on my thesis committee. I thank them for their positive impacts on my education in the graduate school.

I would like to thank my lab mates, who have provided a great support during my research. I would like to acknowledge Xin Zhang for guiding me, teaching me in the beginning of my research. I truly appreciate his efforts in helping me to learn every instruments in our labs and analyzing my experimental results when I just started. I would like to thank Mike Manno, Jeff Walter, Koustav Ganguly, Bryan Voigt for their

suggestions, discussions, helps in my research. I would also want to thank Eric McCalla, Justin Watts, Helin Wang, Alan Albrecht, Ryan Hool for their support and discussions in the group. I want to thank Ming Li, Tianbai Cui, Jiashen Cai, Ruiqi Xing, Yahor Savich, my friends in the physics department for their support, encouragement, and company in my graduate school. They are all intelligent and hard-working people. I wish all the best to them.

Finally, I would like to thank my parents, without their supports and understanding, I cannot even come to the graduate school. I want to thank all my friends for helping me in life and supporting me during my study.

Abstract

Solar energy is a good choice to meet energy and environmental challenges. Researchers have been searching for inexpensive solar absorber materials which can be used in photovoltaic devices. Pyrite FeS_2 has long been recognized as a potential candidate for its high theoretical efficiency, low cost, earth-abundance and non-toxicity. However, the performance of pyrite based solar cells has been limited for some unknown reasons. The poorly understood doping mechanisms have impeded the progress in FeS_2-based solar cell research. Identifying the unknown unintentional dopants, however, remains a big challenge, as does controlled n- and p-type doping. In this work, we explore doping p-type pyrite films via intentional introduction of Mn. We focus on producing p-type films because unintentionally doped films were recently shown to be n-type, likely due to S vacancies. Development of a p-type dopant would therefore enable p-n junctions, a key step in creating a FeS_2-based solar absorber.

Specifically, we synthesized Mn-doped pyrite thin films via *ex situ* sulfidation of $Fe_{1-x}Mn_x$ films. First, a metallic $Fe_{1-x}Mn_x$ thin film was deposited via D. C. magnetron sputtering. Subsequently, this metallic film was sulfidized in a sulfur atmosphere at 600 $^{\circ}C$. We studied the chemical and structural properties of the metallic $Fe_{1-x}Mn_x$ thin films before and after sulfidation. It was found that the $Fe_{1-x}Mn_x$ thin films form a metastable bcc phase, which partly transforms into an fcc phase when the films are

annealed at (or above) 400 $^{\circ}C$. We studied the chemical, structural and electronic transport properties for 10 such films after sulfidation. The Mn-doped pyrite thin films contained nanoscale inhomogeneities which led to hopping transport. None of the thin films were p-type. At high Mn concentrations, we detected the formation of MnS in pyrite FeS_2 films. Though we did not demonstrably succeed in synthesizing phase pure Mn-doped p-type pyrite thin films, the following findings provide insight into how to proceed in the future: we propose to sufidize the $Fe_{1-x}Mn_x$ films in two steps. First, sulfidize the film at a temperature between 200 $^{\circ}C$ and 400 $^{\circ}C$. Subsequently, further anneal this film in sulfur atmosphere at 600 $^{\circ}C$ after all metastable bcc phases convert.

Contents

List of Tables

List of Figures

Chapter 1

Introduction

1.1 Background

Facing global warming by CO_2 emitted from combustion of fossil fuels, the increasing demand for renewable energy has become a major challenge for modern society. Solar energy is a good choice to meet this challenge. Currently, the materials used to make commercial solar cells all have some disadvantages. For example, CdTe, CIGS, etc. contain scarce or toxic materials, while Si-based solar cells remain expensive due to high material costs for thick Si wafers. Hence, the search for better materials to make solar cells that can be deployed on a large scale continues. Pyrite FeS_2 has long been recognized as a potential candidate for its high theoretical efficiency, low cost, earth-abundance and non-toxicity.[1] However, the performance of pyrite-based solar cells has been limited by some unknown reasons.[1] One of the possible reasons for lack

of progress in FeS_2-based solar cells might be the presence of unknown unintentional dopants. Unintentionally doped pyrite FeS_2 films are typically heavily doped and their carrier mobilities are usually very low.[7] On the other hand, the carrier concentration of pyrite single crystals can be five orders of magnitude lower than the films.[7] Unfortunately, identifying these unknown dopants still remains a big challenge. Deliberately doping pyrite n- or p-type in a controlled way is also a serious challenge.

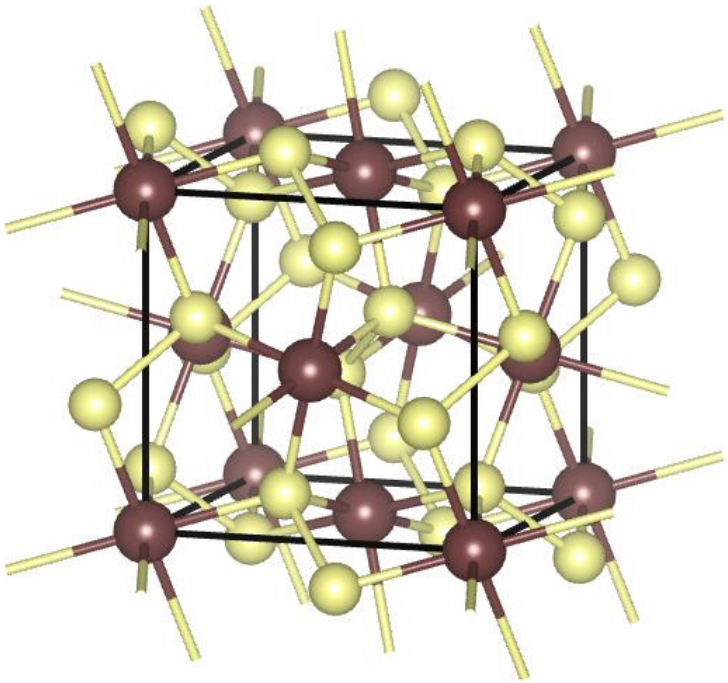

Figure 1.1: Pyrite unit cell, where brown spheres represent iron and yellow spheres represent sulfur.[2]

A considerable amount of research has been done on pyrite FeS_2. It is a common mineral sometimes referred to as "fool's gold". The pyrite structure is shown in figure 1.1. It is widely recognized that unintentionally doped bulk single crystals are n-type.

This is thought to be due to S vacancies.[7] For pyrite thin films, however, researchers used to believe that they were almost always p-type.[1, 3, 4, 5, 6] Recently, Zhang et al. showed that thin films are also n-type and that widespread reports of p-type doping in films with low mobilities are likely due to an artifact in Hall measurements in the presence of hopping transport.[7, 8]

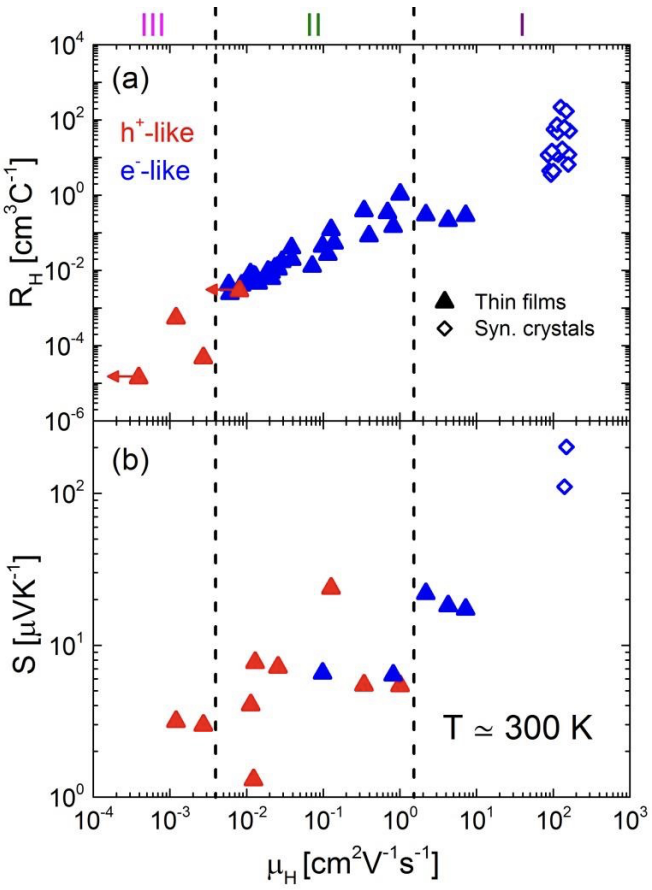

Figure 1.2: The room-temperature (a) Hall coefficient (R_H) and (b) Seebeck coefficient (S) vs. Hall carrier mobility (μ_H) plot for the polycrystalline thin films and synthetic single crystals from Zhang et al.[7]

Zhang et al. based this conclusion on Hall effect and thermopower measurements

on a large set of single crystals and thin films, as shown in fig 1.2. These data can be divided into three regimes according to the Hall mobility. In regime I, the high mobility regime, single crystals and thin films are confirmed to be n-type by both Hall effect and thermopower measurements; in regime II, the intermediate regime, the Seebeck coefficient can reverse sign though the Hall coefficient still shows n-type behavior; and in regime III, the low mobility regime, both Seebeck and Hall coefficients invert. However, this crossover to p-type conduction in the low mobility regime is not truly an n to p crossover. Zhang et al. concluded that the p-type coefficients at low mobility regime is really an artifact of the onset of hopping conduction.[7]

1.2 Motivation

Now that n-type conduction is confirmed in both single crystals and films that are not intentionally doped, two major questions remain. First, what are the unintentional n-type dopants? (Are they indeed S vacancies?) Second, can p-type doping be achieved deliberately? Being able to dope pyrite FeS_2 p-type would be a significant step in FeS_2 research, as, for the first time, p-n homojunctions would be possible (figure 1.3). This would provide a completely new route to FeS_2 solar cells, bypassing the Schottky cells that have underperformed so far.[1]

To dope FeS_2 p-type, the dopant should have one fewer electron than Fe or S. There are thus a lot of choices, but not all of the elements with one fewer electron are possibilities. For example, Cr cannot be incorporated into pyrite FeS_2 under practical

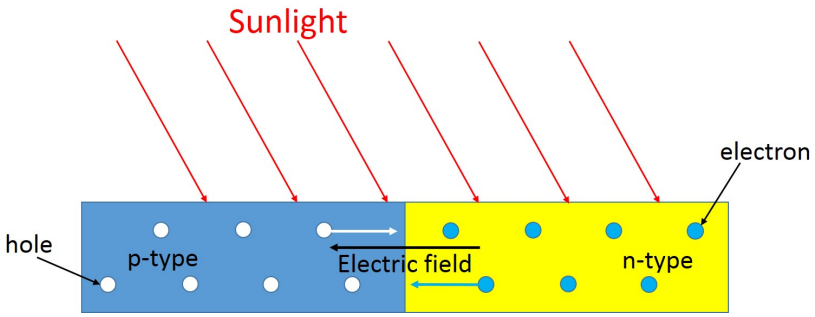

Figure 1.3: A schematic diagram of a p-n junction solar cell.

conditions: extremely high pressure is required.[9] Tc is radioactive, and Re, Sb, Bi etc., are too large to incorporate into pyrite FeS_2. Consulting the literature[10, 11, 12, 13], we narrowed our focus to a small number of possibilities, as shown on the periodic table in figure 1.4. The most relevant literature work is by Lehner et al., who synthesized p-type As-doped pyrite FeS_2 single crystals via chemical-vapor transport.[10] However, As is toxic. Adachi et al. also synthesized $Fe_{1-x}Mn_xS_2$ single crystals with x as large as 0.056 via the $PbCl_2$-flux method.[11] However, Adachi et al. have not studied the electronic properties of these crystals.[11] More recently, Yu et al. also reported that they made Mn-doped pyrite films via chemical bath deposition.[12] However, they did not mention any electronic transport properties of their Mn-doped pyrite films.[12] Mn is a simple choice to start with, since it can be easily introduced into thin film Fe via co-sputtering. We found, however, that this incorporation is not straightforward; neither is the subsequent sulfidation.

In this thesis, we focus on studying Mn-doped Fe thin films before and after sulfidation. In chapter 2, we will introduce the basic experimental methods used. In chapter

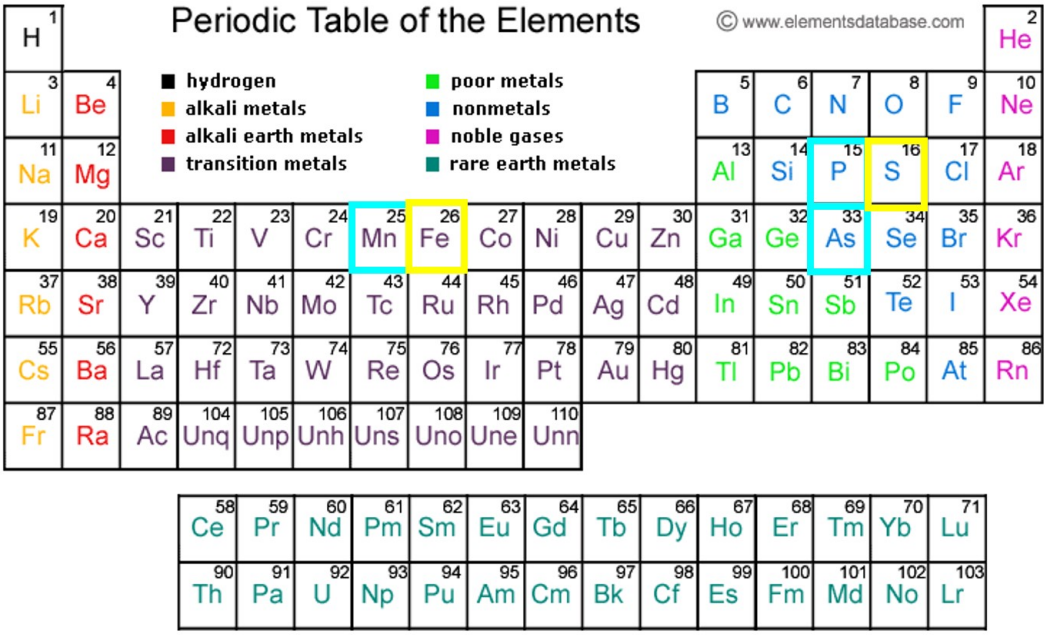

Figure 1.4: Candidates for possible p-type dopants in FeS_2 (elements in blue boxes).

3, we will discuss the chemical and structural properties of $Fe_{1-x}Mn_x$ thin films before sulfidation. Subsequently, in chapter 4, we will discuss the chemical, structural and electronic transport properties of sulfidized $Fe_{1-x}Mn_xS_2$ thin films. Finally, in chapter 5, we will provide a conclusion and some suggestions for future work.

Chapter 2

Experimental Methods

In this chapter, we introduce the basic experimental methods used in this study, including thin film synthesis, characterization and electronic transport measurements.

2.1 Thin Film Synthesis

In this work, thin films were synthesized via a two-step method, *ex situ* sulfidation of metallic thin films. In the first step, a metallic $Fe_{1-x}Mn_x$ film was deposited on a Al_2O_3 (0001) substrate via magnetron sputtering. In the second step, the metallic film from the first step was sulfidized in sulfur vapor, in a closed system at 600 $^{\circ}C$.

2.1.1 Magnetron Sputtering

Magnetron sputtering is a physical vapor deposition process widely used for thin film deposition. During the sputtering process, Ar (or some other inert gas) is supplied

into an initially high vacuum ($\leq 10^{-7}\ Torr$) chamber. The gas pressure is typically maintained between 1 to 100 $mTorr$ during sputtering, which corresponds to mean free paths of hundreds $\mu m's$ for the atoms and molecules in this chamber. Next, a high potential (typically larger than 100 V) is applied to the target, which generates a plasma and ionized Ar gas. These Ar ions from the plasma are attracted and accelerated to the target, which is held at a negative potential. The Ar ions collide with and eject surface atoms off the target which subsequently travel towards, and deposit on the substrate.

In this work, a K. J. Lesker sputtering system was used. $Fe_{1-x}Mn_x$ thin films were deposited via D.C. magnetron co-sputtering, i.e. by sputtering $Fe_{50}Mn_{50}$ and Fe simultaneously (a $Fe_{50}Mn_{50}$ target was used instead of pure Mn since we target low concentrations of Mn in the films.) These metallic thin films were deposited on Al_2O_3 (0001) substrates to form epitaxial films (an out-of-plane epitaxial relationship with Fe(011) / Al_2O_3(0001) is expected)[7], and their thickness were typically 33 nm. The base pressure was typically less than $5 \times 10^{-8}\ Torr$, and during sputtering the Ar gas pressure was usually maintained at 5.5 $mTorr$. The power applied to the Fe and $Fe_{50}Mn_{50}$ targets were typically between 0 and 300 W, and between 6 W to 100 W, respectively. This resulted in total rates that ranged from 0.5 $\AA/s$ to 2.3 $\AA/s$. By varying the sputtering gun powers of $Fe_{50}Mn_{50}$ and Fe, we could adjust the Mn concentration in the thin films, as discussed in section 3.2.

2.1.2 *Ex situ* Sulfidation

After metallic $Fe_{1-x}Mn_x$ films were deposited via D.C. magnetron sputtering, they were placed in an evacuated (10^{-6} $Torr$) quartz tube and sealed with 1.0 ± 0.2 mg S. Subsequently, the ampoule was place in a ceramic holder in a programmable box furnace. Next, the sulfidation temperature was set via the furnace program. Typically, the temperature was ramped up at a rate of 6.5 $°C/min$ from room temperature to 600 $°C$ and maintained at this temperature for 8 h. At the end of this 8 hours the ampoule cooled down naturally in the furnace. This sulfidation condition was chosen based on previous research by Zhang et al. who found that 600 $°C$ was the best sulfidation temperature to synthesize unintentionally doped pyrite FeS_2 thin films via *ex situ* sulfidation. They showed that films synthesized at 600 $°C$ by this method are phase pure and exhibit diffusive transport. According to Zhang et al., the sulfidation starts at 200 $°C$ and the S pressure is about $20 - 50$ $Torr$ during the sulfidation.[7, 8] The film thickness increases to about 110 nm after sulfidation.

2.2 Structural and Chemical Characterization

2.2.1 X-ray Diffraction

X-ray diffraction (XRD) is a common approach to characterize the structure of materials. The wavelength of X-rays is in the range of $0.1 - 100$ $\AA$, which is comparable to the interatomic spacing in solids. Therefore, in X-ray diffraction, incident X-rays

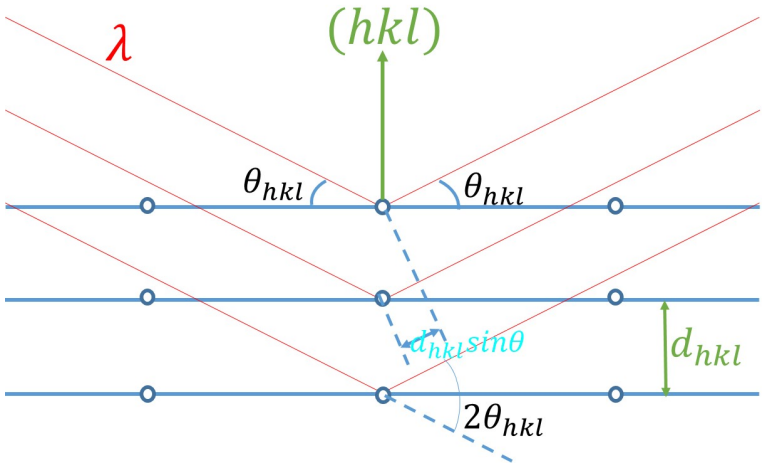

Figure 2.1: A schematic diagram for the elastic scattering of X-ray by atoms.

can be elastically scattered by periodically arranged atoms in a crystal, and thus form a diffraction pattern. From the diffraction pattern, all the crystalline structural information can be obtained. Figure 2.1 shows a typical X-ray scattering diagram, which illustrates the famous Bragg's Law[14],

$$2d_{hkl}sin\theta_{hkl} = n\lambda, \tag{2.1}$$

where d_{hkl} is the interplanar spacing, $2\theta_{hkl}$ is the diffraction angle, n is the order of reflection, and λ is the X-ray wavelength. Bragg's law gives the angles at which constructive interference can occur (the Bragg angle, θ_{hkl}) for a certain set of crystal planes, (hkl). From these angles d_{hkl} can be determined. The lattice parameters can be obtained from d_{hkl}, and most importantly for this work, phases present in these films can be identified.

In this work, both high-resolution X-ray diffraction (HRXRD) and two-dimensional

X-ray diffraction (2DXRD) were used. HRXRD is an X-ray technique where a point detector is used to get the the diffraction intensities for different incident angles. It was used to measure the lattice parameter of epitaxial $Fe_{1-x}Mn_x$ films on Al_2O_3 (0001) in this work. A Panalytical X'Pert Pro with a Cu $K_{\alpha 1}$ X-ray source (wavelength $\lambda = 1.54059\ \mathring{A}$) was used for HRXRD measurements. Typically, a step size of 0.005° and a scan range of $35° - 55°$ was used for the metallic thin films. In contrast, 2DXRD is a technique where an area detector is used. A "diffraction cone" (or "Debye ring") is formed for a polycrystalline sample in 2DXRD. 2DXRD was used for studying the polycrystalline $Fe_{1-x}Mn_xS_2$ thin films. A Bruker D8 Discover 2D with a Co $K_{\alpha 1}$ X-ray source (wavelength $\lambda = 1.78899\ \mathring{A}$) was used for 2DXRD measurements.

2.2.2 Grazing Incidence X-ray Reflectivity

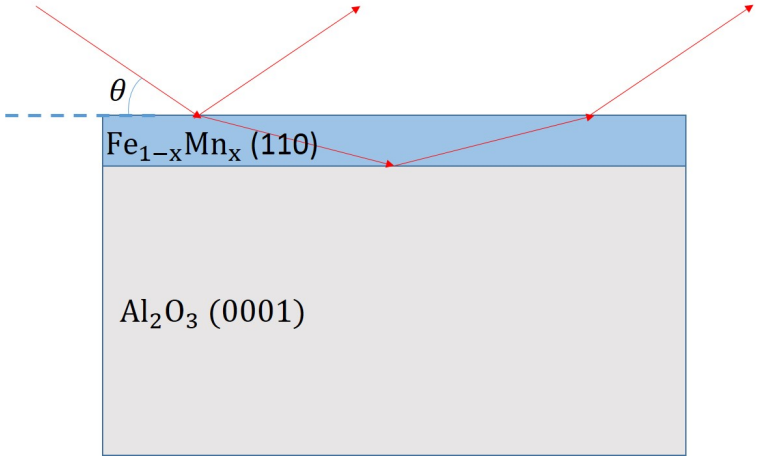

Figure 2.2: A schematic diagram for the grazing incidence X-ray reflectivity measurement.

Grazing incidence X-ray reflectivity (GIXR) is a tool to study the surface and layer

thickness in thin films. In this work, it was used to measure the film thickness. As shown in figure 2.2, an X-ray beam with a very small incident angle ($< 10°$) is reflected by both the film surface and the interface between the film and the substrate. The interference of these reflected beams form fringes in the reflected X-ray intensity. The thickness of the thin film can be found from the modified Kiessig formula[7, 15],

$$sin^2\theta_N = \frac{\lambda^2}{4t^2}N^2 + sin^2\theta_C, \tag{2.2}$$

where θ_N is the angle at which the X-ray intensity is maximum, λ is the X-ray wavelength, t is the film thickness, N is the Kiessig fringe order integer, and θ_C is the critical incident angle (a constant for a given material). Fitting $sin^2\theta_N$ vs. N^2 with a straight line, one can calculate the film thickness from the slope. The sputtering rate was determined by measuring the thickness of thin films deposited for a certain time period, Δt, and dividing the thickness by Δt. A Panalytical X'Pert Pro with a Cu $K_{\alpha 1}$ X-ray source (wavelength $\lambda = 1.54059\ \mathring{A}$) was used for GIXR measurements. Typically, a step size of $0.005°$ and a scan range of $0.2° - 8°$ was used in the measurements.

2.2.3 Scanning Electron Microscopy and Energy Dispersive Spectrosco -py

We use scanning electron microscopy (SEM) to study the surface morphology of our films. When an electron beam is incident on a sample, the scattered or generated electrons reveal information including the surface morphology and the chemical composition of the sample. The secondary electron (SE) is sensitive to the surface morphology

of samples. Hence, we use the secondary electrons images (SEI) in this work.

Energy dispersive spectroscopy (EDS) is typically installed on SEMs to enable elemental composition measurements. In EDS, an incident electron knocks out a core electron from the atoms in the sample. Subsequently, an outer electron relaxes to the lower energy state and emits an X-ray. From the intensity and energies of the emitted X-rays (the EDS spectrum), the elements present in the sample can be identified and the sample composition can be determined. In this work, the chemical composition of thin films both before and after sulfidation were determined via EDS. A JEOL 6500 Field Emission Gun Scanning Electron Microscope was used for SEM and EDS measurements. Typically, SEI was chosen for the SEM imaging mode; an accelerating voltage of 20 kV and a working distance of 10 mm were used for both SEM and EDS.

2.2.4 Raman Spectroscopy

Raman spectroscopy is a technique that relies on inelastic light scattering to identify atomic vibrations in films and molecules. In Raman scattering, an incident photon excites electrons to a virtual state, then in some cases this electron will relax to a different state instead of its original state, in this process a photon with a frequency shift will be emitted. If the frequency shift is negative, we call it an Anti-Stokes Shift; while if it is positive, we call it a Stokes Shift. In this work, Raman spectroscopy was used as a complementary technique to confirm the phase purity in pyrite thin films since it is very sensitive to some impurities such as marcasite. A Witec Alpha300R Confocal

Raman Microscope was used in Raman spectroscopy measurements. Typically, in our measurements the wavelength was 514.5 nm and the laser spot size was in the order of 1 μm in diameter.

2.3 Electronic Transport Measurements

Electronic transport measurements included temperature-dependent resistivity measurements and Hall effect measurements. They are essential in understanding the transport properties and doping in pyrite thin films.

2.3.1 Temperature-dependent Resistivity Measurements

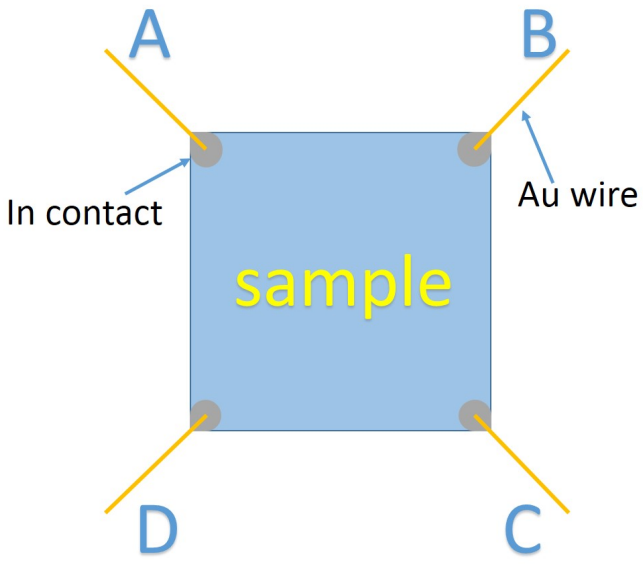

Figure 2.3: van der Pauw configuration for temperature-dependent resistivity measurements.

The van der Pauw method[16], a four-terminal method with very few limitations on the sample, was used to measure the temperature-dependent resistivity of Mn-doped pyrite films. As shown in figure 2.3, four Ohmic In contacts are made on the corners of the sample; a Au wire connects each contact with the probe. In a four terminal resistance measurement a source current is applied through one side, and voltage is measured on the other side. The voltage divided by the current is the four-terminal resistance in this configuration. For example, if the source current is applied from A to B (I_{AB}), and the voltage is measured between D and C (V_{DC}), then the four-terminal resistance in this configuration is,

$$R_{AB,DC} = \frac{V_{DC}}{I_{AB}}. \tag{2.3}$$

The four-terminal resistance for another configuration, for example $R_{AD,BC}$, can be measured in a similar way. By solving the van der Pauw equation,

$$e^{-\pi R_{AB,DC}/R_S} + e^{-\pi R_{AD,BC}/R_S} = 1, \tag{2.4}$$

the sheet resistance (R_S) of the sample is determined. The resistivity is given by

$$\rho = R_S t, \tag{2.5}$$

where t is the film thickness. By varying the temperature, the resistivity at different temperatures, $\rho(T)$, can be obtained.

In this work, a Quantum Design Physical Property Measurement System (PPMS) is used. The sample temperature can be controlled between 1.9 $K - 400$ K in this

PPMS. Typically, in this work the resistivity, $\rho(T)$, for most samples was measured from $T \leq 15\ K$, where the sample resistance become too large to be measured, to $T = 300\ K$. (In our measurements, one configuration was measured while cooling and the other configuration was measured while heating. The resistivity $\rho(T)$ was calculated from equations (2.4) and (2.5).) At different temperatures, the applied current was selected based on the four-terminal I-V curves: we chose the highest possible current while the conduction was still Ohmic.

2.3.2 Hall Effect Measurements

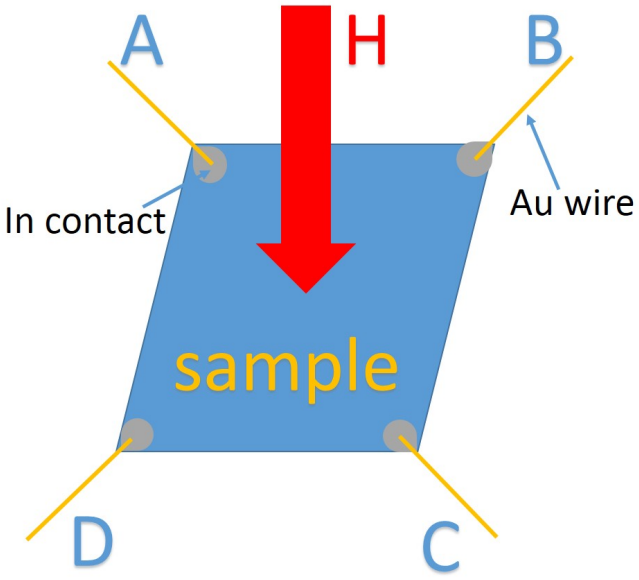

Figure 2.4: A schematic diagram for Hall effect measurements

Hall effect measurements were used to study the electronic transport mechanism in

doped and undoped pyrite films. Hall effect measurements can reveal the carrier type, carrier concentration and mobility. The configuration is very similar to the van der Pauw configuration mentioned previously. The only differences is that there is now a magnetic field applied to the sample and the directions for applied current and measured voltage are different. As shown in figure 2.4, a perpendicular magnetic field (H) is applied to the sample, a source current is applied through A, C (I_{AC}), and the Hall voltage that develops between D and B is measured (V_{DB}). In Hall measurements, the magnitude and direction of the magnetic field (H) is changed, and the voltage (V_{DB}) as a function of magnetic field (H) is measured. The Hall coefficient (R_H) can be expressed as

$$R_H = \frac{V_{DB}t}{I_{AC}} \cdot \frac{1}{H} \equiv \frac{\rho_{xy}}{H}, \tag{2.6}$$

where t is the sample thickness and $\rho_{xy} = V_{DB}t/I_{AC}$ is defined as the Hall resistivity. The carrier type can be found from the sign of R_H: for holes R_H is positive, and for electrons it is negative. The carrier (hole or electron) concentration can be calculated from

$$p \ (or \ n) = \frac{1}{eR_H}, \tag{2.7}$$

where p is the hole concentration, n is the electron concentration, (one dominant carrier is assumed here), and e is the electron charge. Similarly, the carrier mobility (μ_e for electrons, μ_h for holes) is given by

$$\mu_e \ (or \ \mu_h) = \frac{1}{n \ (or \ p) \ e\rho}, \tag{2.8}$$

where ρ is the sample resistivity.

In this work, the same PPMS mentioned in the previous section was used for the Hall effect measurements. In the measurement, the magnetic field was swept from 9 T to -9 T, the temperature was kept constant typically at 290 K, and the Hall resistance for different magnetic fields was measured. The applied current we selected was typically the largest possible current in the Ohmic regime of the I-V curve in the Hall configuration. The carrier type, concentration and mobility were obtained from equations (2.6) to (2.8).

2.3.3 Magnetometry

In this work, we used a Quantum Design Magnetics Property Measuring System (MPMS) XL, a superconducting quantum interference device (SQUID) magnetometer, to measure the magnetic behavior of $Fe_{1-x}Mn_x$ thin films. A SQUID uses the magnetic flux quantization through a superconducting loop based on a Josephson junction to measure the magnetic moment in a material.[17] It is a very sensitive measurement for very small magnetic moments.

Chapter 3

Synthesis and Characterization of $Fe_{1-x}Mn_x$ Thin Films Before Sulfidation

As introduced in previous chapters, the pyrite $Fe_{1-x}Mn_xS_2$ thin films in this work were synthesized via a two-step method, where, in the first step, metallic $Fe_{1-x}Mn_x$ thin films were deposited via magnetron sputtering. To ensure the homogeneity and phase purity of the final pyrite $Fe_{1-x}Mn_xS_2$ thin films in the second step, it is important to study the metallic films before sulfidation. This chapter presents a detailed study of the metallic $Fe_{1-x}Mn_x$ thin films deposited via magnetron sputtering. We found that these films are in a metastable bcc phase. We also showed that these films in this metastable

bcc phase partly transformed into an fcc phase after annealing at (or above) 400 $°C$.

3.1 Phase Diagram of $Fe_{1-x}Mn_x$

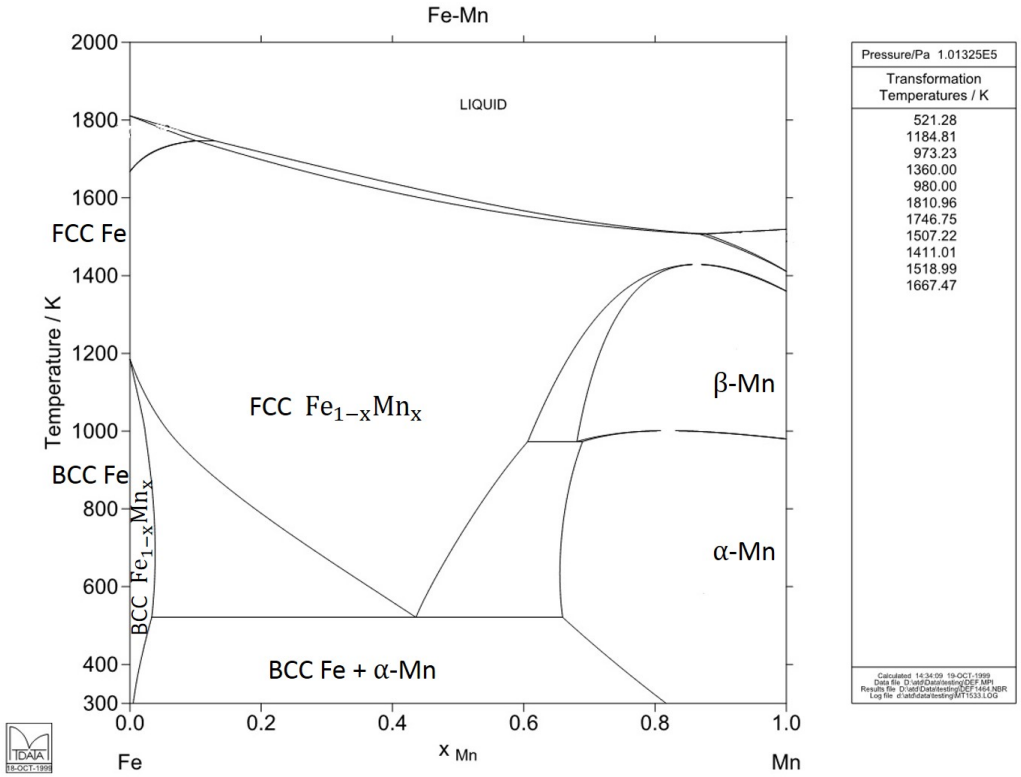

Figure 3.1: Equilibrium phase diagram of $Fe_{1-x}Mn_x$[18]

As shown in figure 3.1, the equilibrium phase diagram of $Fe_{1-x}Mn_x$ is quite complex. Because we aim to incorporate very low Mn concentrations, perhaps 2% or below, we were especially interested in the very left body centered cubic (bcc) regime on this phase diagram where the Mn concentration is at most several percent (assuming Mn

will be electrically activated). Since sputtering is an energetic process, the equilibrium phase diagram, while a useful guide, may not be entirely applicable and metastable phases may be produced. For example, it is well known that $Fe_{50}Mn_{50}$ films deposited via R.F. sputtering at room temperature are in the face centered cubic (fcc) phase.[19] Nevertheless, the equilibrium phase diagram is a good starting point. To get a comprehensive understanding of the phases present in these sputtered $Fe_{1-x}Mn_x$ thin films, we deposited and studied films with different Mn concentrations between 0 and 50% at both 20 $^{\circ}C$ and 300 $^{\circ}C$.

3.2 Chemical Composition of Our $Fe_{1-x}Mn_x$ Thin Films

In this work, the $Fe_{1-x}Mn_x$ thin films were deposited via co-sputtering of Fe and $Mn_{50}Fe_{50}$. The Mn concentration was controlled by adjusting the co-sputtering powers of the Fe gun and $Mn_{50}Fe_{50}$ gun. The sputtering rate increases linearly with gun powers. Knowing the atomic number densities of Fe and Mn, the concentration of Mn can be predicted.

The sputtering rates at different gun powers were determined by measuring, via GIXR, the thickness of films deposited at certain sputtering gun power for a certain time period. For each sputtering gun power value, the thickness of the film divided by the deposition time is the deposition rate at this power. As shown in figure 3.2, the sputtering rate of $Mn_{50}Fe_{50}$ increased linearly with the gun power. The sputtering rate of the Fe target were also measured at 100 W and 300 W in the same way, and assumed

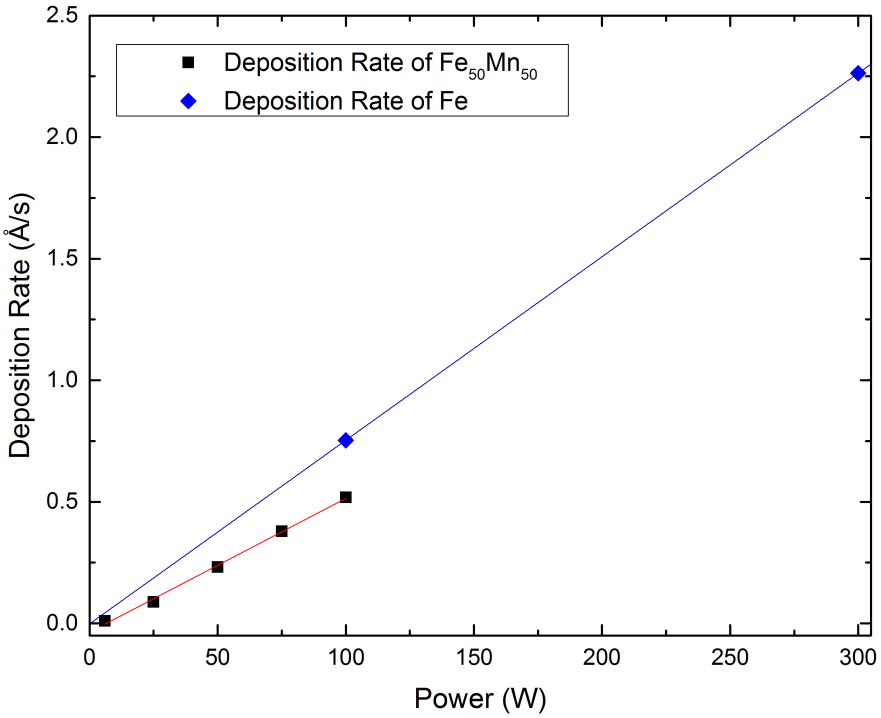

Figure 3.2: Linear relationship between the sputtering rate and power. ■: for $Fe_{50}Mn_{50}$ target, ♦: for Fe target. All of them were deposited on Al_2O_3 (0001) substrate at 20 $^{\circ}C$, and the Ar pressure were at 5.5 $mTorr$.

to change linearly. During co-sputtering, the gun power for the Fe target was usually set at 0 W, 100 W or 300 W, and the gun power for the $Mn_{50}Fe_{50}$ target was chosen to produce a film with the desired Mn concentration. The expected Mn concentrations were based on the linear relationships between the gun powers and deposition rates in figure 3.2. Theoretically, we can dope our films with Mn in the $0.2\% \sim 50\%$ range, where the lower limit, 0.2%, is limited by the lowest gun power to stabilize the $Fe_{50}Mn_{50}$ target. For example, table 3.1 shows some specific predicted rates based on the gun powers for the Fe and $Fe_{50}Mn_{50}$ targets. After deposition, the thicknesses of the thin films were

confirmed using GIXR, which agreed with the predictions.

Table 3.1: Predicted Mn concentration based on the gun powers of Fe and $Fe_{50}Mn_{50}$ targets.

Gun power for Fe target	Gun power for $Fe_{50}Mn_{50}$ target	Predicted Mn Atomic Ratio
300 W	6 W	0.2%
300 W	12 W	0.6%
300 W	25 W	1.8%
300 W	37 W	3.4%
300 W	100 W	9.2%
100 W	100 W	20.0%
0 W	100 W	50.0%

Table 3.2: Comparison of the predicted and measured Mn concentration.

Sample	Predicted Mn Atomic Ratio	Measured Mn Atomic Ratio from EDS
016d	20%	20.5%
016e	20%	18.9%
FeMn10	50%	51.9%

In addition, for Mn concentration higher than about 10%, the concentration can be directly measured using EDS. As shown in table 3.2, the prediction of the Mn concentration agrees with EDS measurements very well. Since EDS is only reliable for high concentrations of elements, the EDS measurements for low Mn concentration (less than 20%) samples are not shown here. EDS spectra were collected from several different regions for each film. The EDS data from different regions of the film confirmed its compositional homogeneity on large length scales. For example, figure 3.3 shows

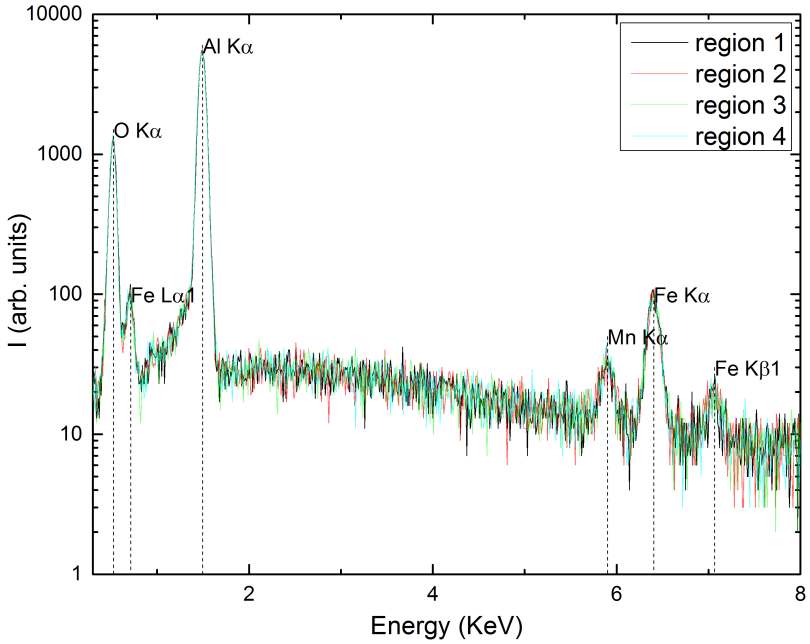

Figure 3.3: EDS spectra for four different regions of a $Fe_{0.8}Mn_{0.2}$ thin film. The accelerating voltage were 20 kV, working distance were 10 mm, the areas of regions 1, 2, 4 were about 300 μm^2, and area of region 3 was about 1200 μm^2.

EDS spectra collected from four different regions of a $Fe_{0.8}Mn_{0.2}$ thin film separated by approximately 0.1 mm. These spectra were almost identical, which confirms the homogeneity of this film. Similar confirmations were done for other thin films. It can be concluded that these $Fe_{1-x}Mn_x$ thin films have a macroscopically uniform distribution of Mn, and the measured Mn concentration agrees with the prediction from co-sputtering rate. Mn is thus well incorporated in the thin films chemically, but what is the crystal structure?

3.3 Structural Properties

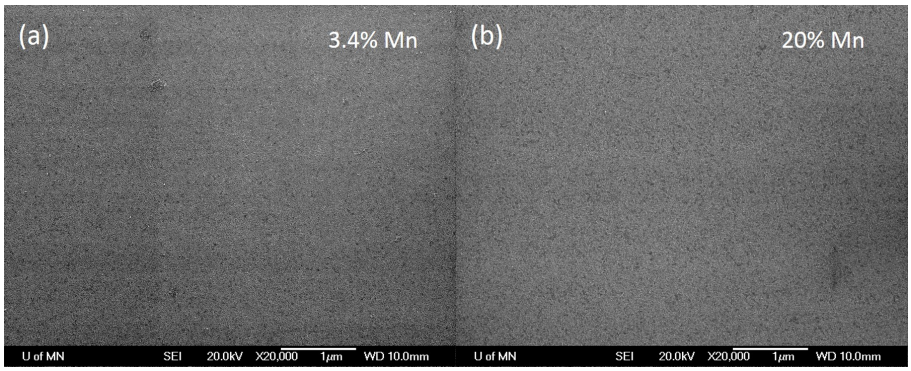

Figure 3.4: (a) SEM image (SEI) of the surface of a $Fe_{0.966}Mn_{0.034}$ thin film. (b) SEM image (SEI) of the surface of a $Fe_{0.8}Mn_{0.2}$ thin film.

SEM images of these $Fe_{1-x}Mn_x$ thin films show that they are smooth and continuous. There is no visible difference between films of different Mn concentrations. For example, figure 3.4 (a) shows a film with 3.4% Mn, while figure 3.4 (b) shows a film with 20% Mn. One could not distinguish them from their SEM images.

On the other hand, XRD proves very informative for these $Fe_{1-x}Mn_x$ thin films. XRD data as a function of Mn concentration is shown in figure 3.5. All the films that contain 20% or less Mn were deposited at 300 $^{\circ}C$ and characterized via HRXRD. The film containing 30% Mn was deposited at 20 $^{\circ}C$ and also characterized via HRXRD. The film containing 50% Mn was deposited at 20 $^{\circ}C$ and characterized using 2DXRD. According to these data, it appears that all of these films are phase pure and exhibit an XRD pattern very close to a body centered cubic (bcc) structure, except the film with 50% Mn, which shows a face centered cubic (fcc) pattern. As mentioned before,

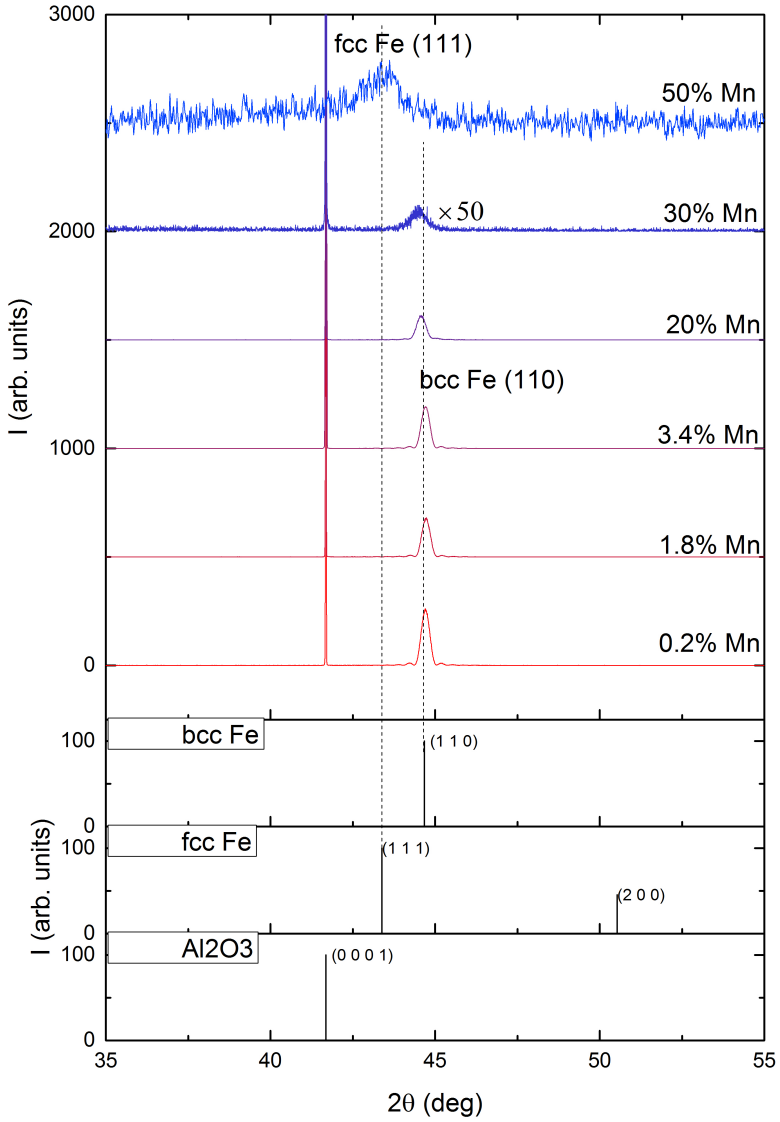

Figure 3.5: XRD data as a function of Mn concentration. The 50% Mn film was deposited at 20 $^{\circ}C$ and characterized via 2DXRD. The 30% Mn film was deposited at 20 $^{\circ}C$ and characterized via HRXRD. The rest of the films were deposited at 300 $^{\circ}C$ and characterized via HRXRD.

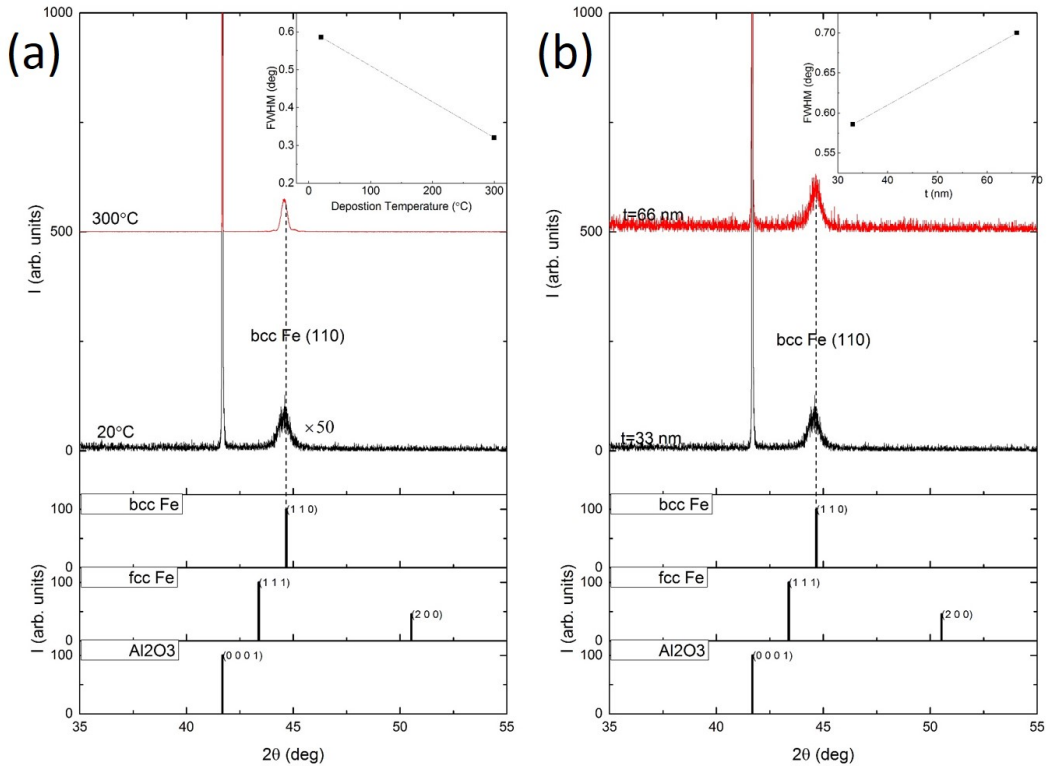

Figure 3.6: (a) XRD data for two 33 nm-thick films containing 20% Mn deposited at 20 $°C$ and 300 $°C$, respectively; (b) XRD data for two films containing 20% Mn deposited at 20 $°C$ with thickness 33 nm and 66 nm, respectively. The insert figures show the FWHM of the peak width.

fcc is expected at 50% Mn. The XRD patterns in figure 3.5 show that our $Fe_{1-x}Mn_x$ thin films have bcc structure with x up to 0.3. However, this is contrary to expectations from the equilibrium phase diagram shown in figure 3.1. Is this some non-equilibrium Fe-Mn solid solution, or phase separation with some undetected Mn-rich phase? We address this question next.

Lowering the deposition temperature or increasing the film thickness were found

not to change the peak position in the XRD patterns, but only affect the peak width. Figure 3.6 (a) shows the XRD patterns for two 33 nm-thick films containing 20% Mn deposited at 20 $^{\circ}C$ and 300 $^{\circ}C$, respectively, while figure 3.6 (b) shows the XRD patterns for two films containing 20% Mn deposited at 20 $^{\circ}C$ with thicknesses 33 nm and 66 nm, respectively. The peak positions remained constant while the peak widths increased when the deposition temperature was lowered (see inset in figure 3.6 (a)). Increasing the film thickness also increased the peak widths (see inset in figure 3.6 (b)). From the widths of the XRD peaks we can find the grain size using the Scherrer equation[20],

$$\tau = \frac{K\lambda}{\beta cos\theta}, \tag{3.1}$$

where τ is mean size of the crystalline domains, K is a dimensionless shape factor, λ is the X-ray wavelength, β is the line broadening at half the maximum intensity (FWHM), and θ is the Bragg angle. Lowering the deposition temperature from 300 $^{\circ}C$ to 20 $^{\circ}C$ decreased the out of plane grain size τ from 270 $\mathring{A}$ to 150 $\mathring{A}$. While, increasing the film thickness from 33 nm to 66 nm decreased the out of plane grain size τ from 150 $\mathring{A}$ to 120 $\mathring{A}$. We note that these are rough estimates as microstrain is ignored.

If we calculate the lattice parameters of these thin films from the XRD data by assuming bcc structures for all of them, we find that the lattice parameters do not follow Vegard's Law[21] between bcc Fe and hypothetical bcc Mn as the Mn concentration increases (figure 3.7). The XRDs show a bcc diffraction pattern at least up to 30% Mn, with only a very weak increase in lattice parameter, far below the prediction from Vegard's Law (the green line in figure 3.7). There are two possibilities: (1) there might

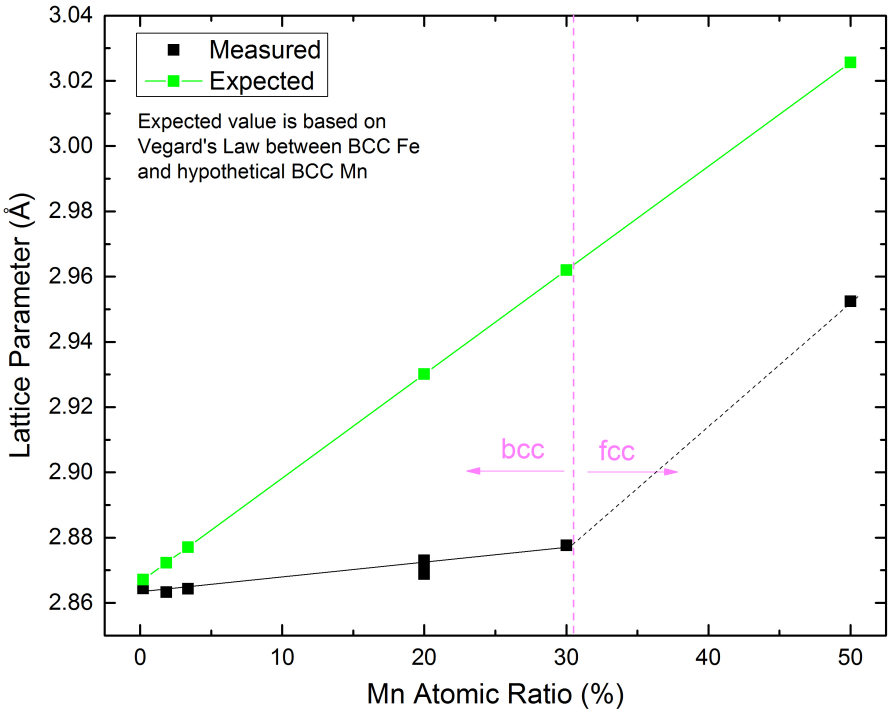

Figure 3.7: Comparison of measured lattice parameters and predicted lattice parameters from Vegard's Law between bcc Fe and hypothetical bcc Mn.

be some Mn in a phase undetectable by XRD, for example, in amorphous form so that we always measure a lattice parameter nearly the same as that of bcc Fe; or more likely (2) these alloys violate Vegard's Law as has been reported previously.[22, 23, 24]

3.4 Metastable bcc $Fe_{1-x}Mn_x$ Solid Solution Films

To determine whether Mn is segregated as a different phase, we conducted 2DXRD measurements for several films with 20% Mn, but neither a secondary phase nor any indication of amorphous Mn, where very broad peaks are typically shown in the XRD

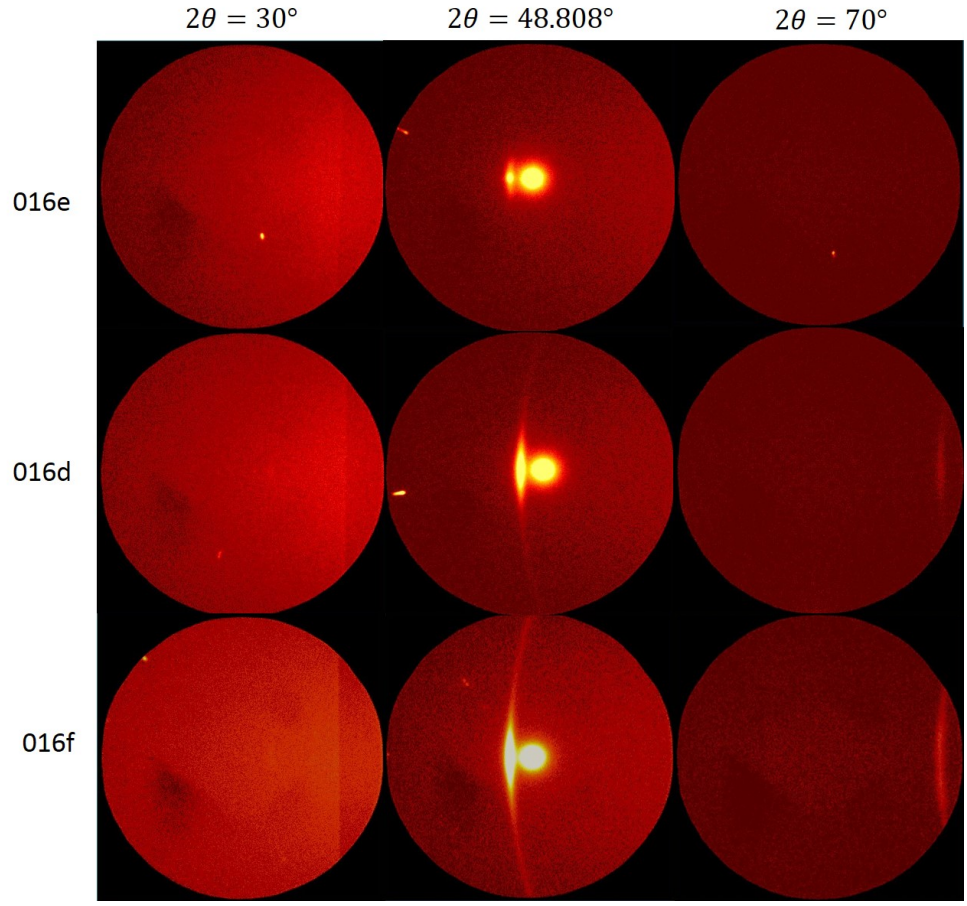

Figure 3.8: 2DXRD data. 016e: a 33 nm-thick $Fe_{0.8}Mn_{0.2}$ thin film deposited at 300°C, 016d: a 33 nm-thick $Fe_{0.8}Mn_{0.2}$ thin film deposited at 20°C and 016f: a 66 nm-thick $Fe_{0.8}Mn_{0.2}$ thin film deposited at 20°C

pattern, were found. Figure 3.8 shows, from top to bottom, three different films containing 20% Mn. Film 016e was 33 nm thick and was deposited at 300°C, film 016d was 33 nm thick and was deposited at 20°C, and film 016f was 66 nm thick and was deposited at 20°C. From left to right figure 3.8 shows three different frames scanned for each film with the frame center set at $2\theta = 30°$, 48.808°, and 70°, respectively. The bcc-Fe phase was detected in all these films. We therefore find that our $Fe_{1-x}Mn_x$ films

with x up to 0.3 are bcc and a solid solution of Fe and Mn. While this is surprising, precedent exists, as we now discuss.

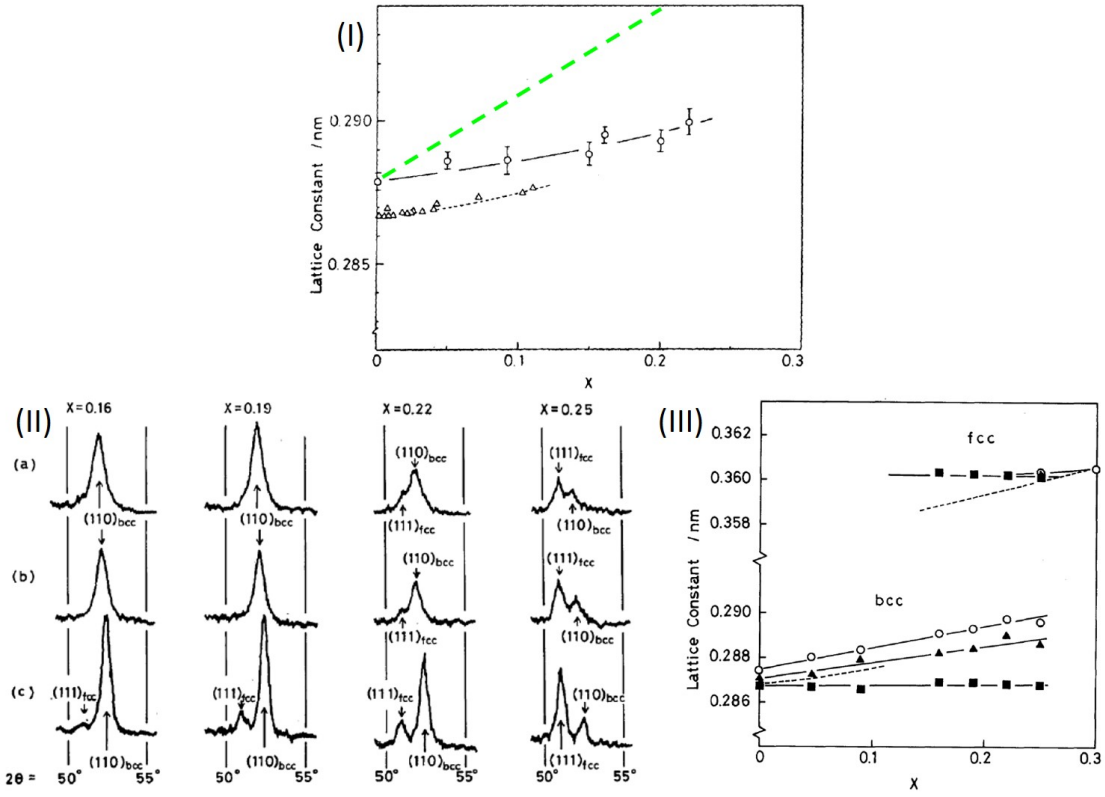

Figure 3.9: (I) Lattice parameters of the bcc $Fe_{1-x}Mn_x$ alloys. ○: sputtered alloy films by Sumiyama et al., △: the bulk alloys.[22] The dashed line is the trend of lattice parameters according to Vegard's Law. (II) XRD patterns of the sputtered $Fe_{1-x}Mn_x$ alloy films by Sumiyama et al. (a) as-sputtered alloys, (b) after annealing at 470 K for two hours and (c) after annealing at 670 K for two hours, respectively.[23] (III) Lattice parameters of the $Fe_{1-x}Mn_x$ alloys by Sumiyama et al. ○: sputtered alloys, as sputtered, ▲: those after annealing at 470 K for two hours and ■: those after annealing at 670 K for two hours.[23]

Specifically, according to Sumiyama et al., there exists a metastable bcc $Fe_{1-x}Mn_x$ solid solution, where x can be up to and even more than 0.2. In fact, they synthesized this metastable phase via sputtering.[22, 23, 24] Their lattice parameters also did not

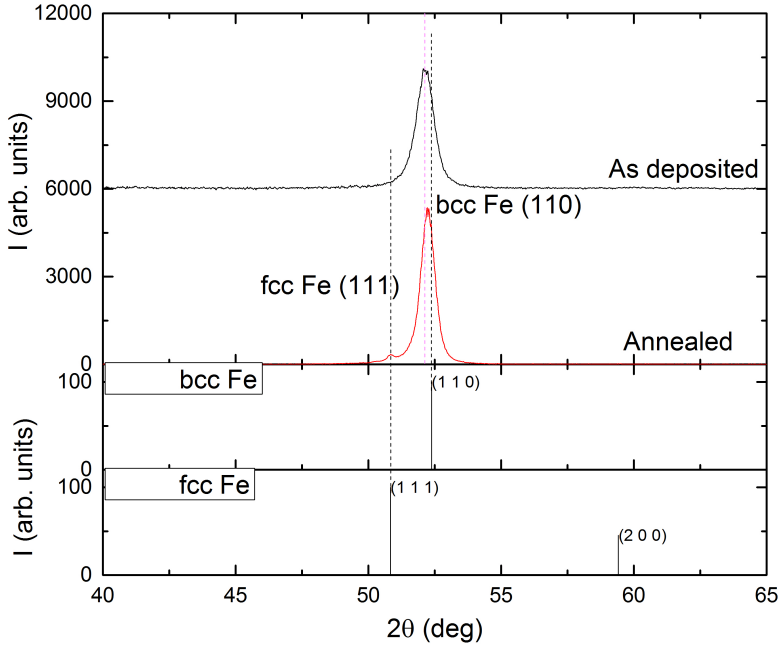

Figure 3.10: XRD patterns for a $Fe_{0.7}Mn_{0.3}$ thin film deposited at 20 $^{\circ}C$ before and after annealing at 400 $^{\circ}C$ for 2 h. 2DXRD was used in this measurement.

follow Vegard's Law. As shown in figure 3.9 (I)[22], the measured lattice parameters were significantly lower than those predicted by Vegard's Law (the green dashed line in the figure). They showed that after annealing at 670 K (397 $^{\circ}C$) for two hours, the metastable bcc phase partly transforms to the fcc phase, and the bcc peak position shifts towards higher 2θ, i.e., towards the diffraction peak location for pure Fe.[23] Figures 3.9 (II) and (III)[23] show the XRD patterns after annealing, and the lattice parameters calculated from these XRD data. Clearly, this group obtained metastable $Fe_{1-x}Mn_x$ alloy films via sputtering, although no explanation was provided for the existence of the metastable phase or the violation of Vegard's Law. These films were stable only at

low temperatures. When the temperature was increased above 400 $^{\circ}C$ the films phase separated into a mixed phase of bcc and fcc phases.

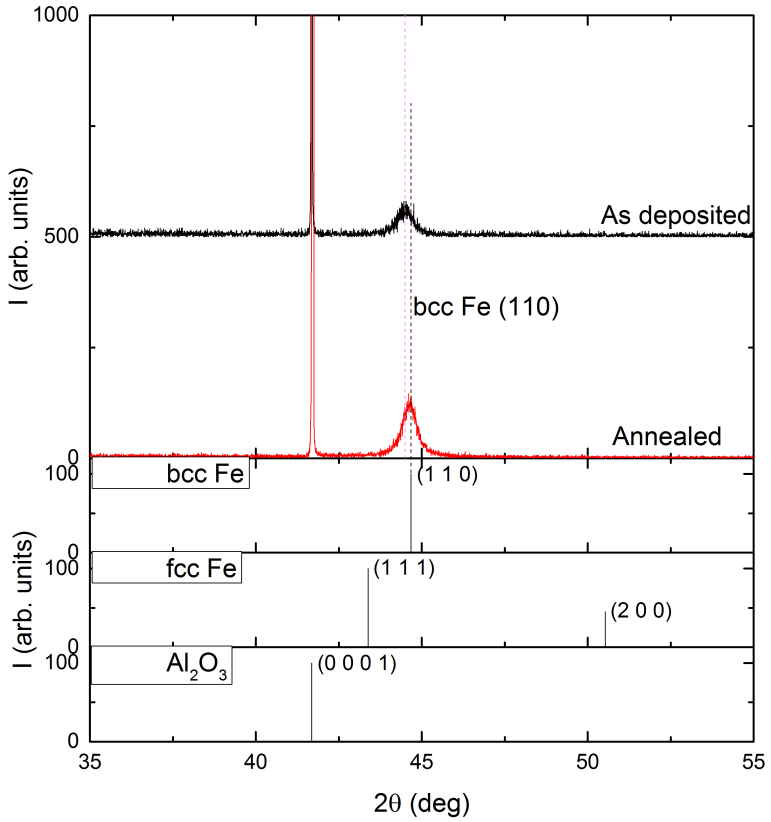

Figure 3.11: XRD patterns for a $Fe_{0.7}Mn_{0.3}$ thin film deposited at 20 $^{\circ}C$ before and after annealing at 400 $^{\circ}C$ for 2 h. HRXRD was used for this measurement.

Is the situation similar in our case? An $Fe_{0.7}Mn_{0.3}$ thin film deposited at 20 $^{\circ}C$ was annealed in vacuum at 400 $^{\circ}C$ for two hours. Figure 3.10 shows the XRD patterns before and after annealing for this film. A small but clear fcc peak shows up after annealing. Thus, the phase separation observed by Sumiyama et al. is also happening in our case. In addition, we used HRXRD to determine the lattice parameters for the

bcc phase before and after the annealing. As shown in figure 3.11 and as expected, the bcc (110) peak shifted to higher 2θ after annealing. Meanwhile, the lattice parameter decreased from 2.878 $\mathring{A}$ to 2.869 $\mathring{A}$. For comparison, the lattice parameter for pure Fe is 2.866 $\mathring{A}$.

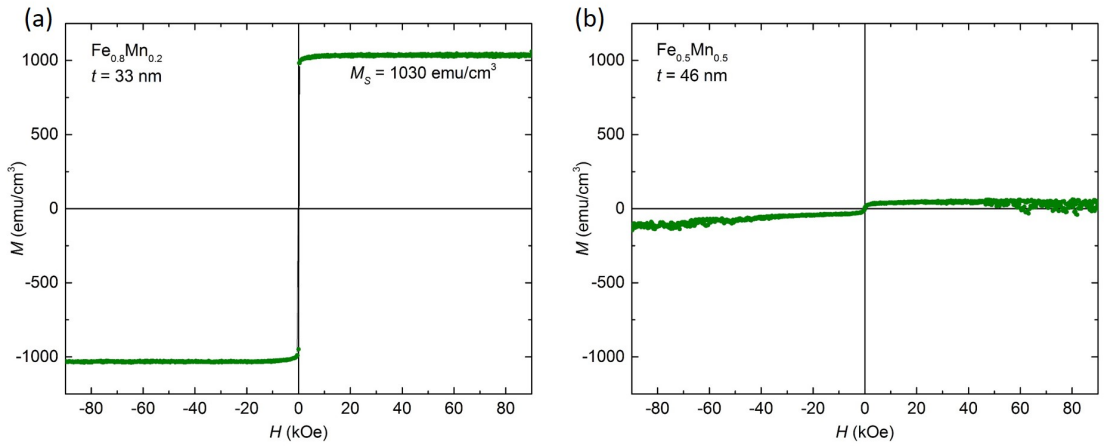

Figure 3.12: Field dependence of magnetization for (a) a $Fe_{0.8}Mn_{0.2}$ film and (b) a $Fe_{50}Mn_{50}$ film.

In addition, we also conducted magnetometry measurements for some films. Figure 3.12 shows the field dependence of magnetization for (a) an $Fe_{0.8}Mn_{0.2}$ film and (b) an $Fe_{50}Mn_{50}$ film. Figure 3.12 (a) shows that the bcc $Fe_{0.8}Mn_{0.2}$ film has a magnetization of 1030 emu/cm^3 or 132 emu/g (taking the density of $Fe_{0.8}Mn_{0.2}$ as 7.785 g/cm^3), which agrees perfectly with Sumiyama et al.'s measurements, which are shown in figure 3.13.[22] Figure 3.12 (b) shows that the fcc $Fe_{50}Mn_{50}$ film exhibits anti-ferromagnetism and has little magnetization. This is well known. This finding reinforced our hypothesis that we obtained a metastable bcc solid solution of Fe-Mn similar to that synthesized by Sumiyama et al.

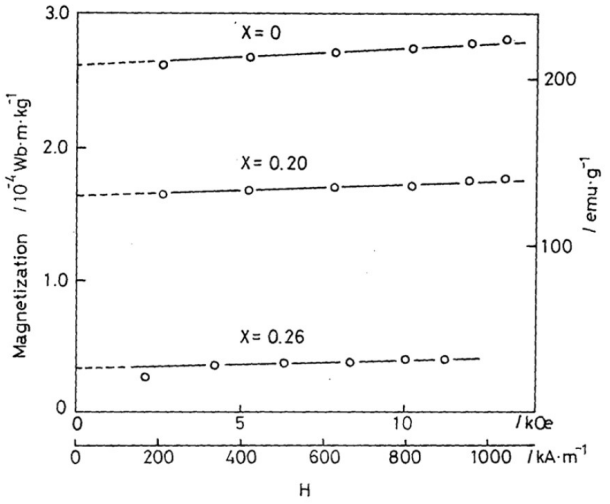

Figure 3.13: Field dependence of magnetization for the films by Sumiyama et al.[22]

It can thus be concluded that the $Fe_{1-x}Mn_x$ ($x < 0.3$) thin films deposited via sputtering in this work are actually metastable bcc solid solutions. This metastable phase is trapped during sputtering, which extends the solubility of Mn into Fe up to about 30%. This metastable phase separates into mixed phases of bcc and fcc structure at temperatures higher than 400 $°C$. This metastable bcc solid solution is indeed a promising starting point for the next step, *ex situ* sulfidation, though we did not know the fact that the phase separation starts at 400 $°C$ before we sulfidized them at 600 $°C$. We will see what will happen after the sulfidation in next chapter.

Chapter 4

Characterization and Electronic Transport Properties of Mn-doped Pyrite Thin Films

In the previous chapter, we found that the non-equilibrium $Fe_{1-x}Mn_x$ metastable bcc solid solution is potentially promising for being sulfidized and forming phase pure Mn-doped pyrite thin films. This chapter will provide a systematic study of the structural, chemical, and electronic transport properties of these $Fe_{1-x}Mn_xS_2$ films we obtained from sulfidation.

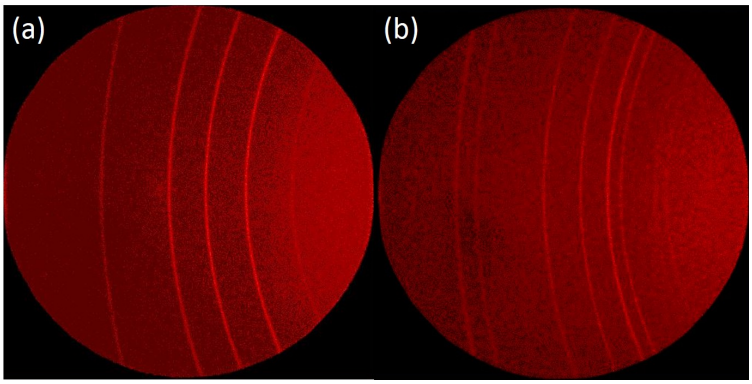

Figure 4.1: Debye rings acquired from 2DXRD. (a) is a thin film containing 0.2% Mn. (b) is a thin film containing 50% Mn, a polycrystalline secondary phase is obvious.

4.1 Structural and Chemical Properties

All the $Fe_{1-x}Mn_x$ films used for sulfidation studies were first deposited at 20 $°C$ or 300 $°C$ on Al_2O_3 (0001) substrates via D.C. magnetron sputtering. They were all initially 33 nm thick and sulfidized at 600 $°C$. Upon sulfidation, 110 nm-thick $Fe_{1-x}Mn_xS_2$ thin films were obtained. This sulfidation condition was optimized by Zhang et al. for pure FeS_2.[7, 8] (refer to section 2.1 for more details).

XRD reveals the structural properties and the phase purity of these thin films. Debye rings acquired from 2DXRD showed that the sulfidized films are polycrystalline (as in figure 4.1 for example). By integrating the 2DXRD data, XRD patterns shown in figure 4.2 as a function of Mn concentration, were obtained. Figure 4.2 shows that films containing high concentrations of Mn (20% and 50%) resulted in the formation of MnS in addition to pyrite FeS_2. Films with no visible MnS peaks in their XRD patterns may still have a small amount of MnS present, but this is difficult to observe and detect.

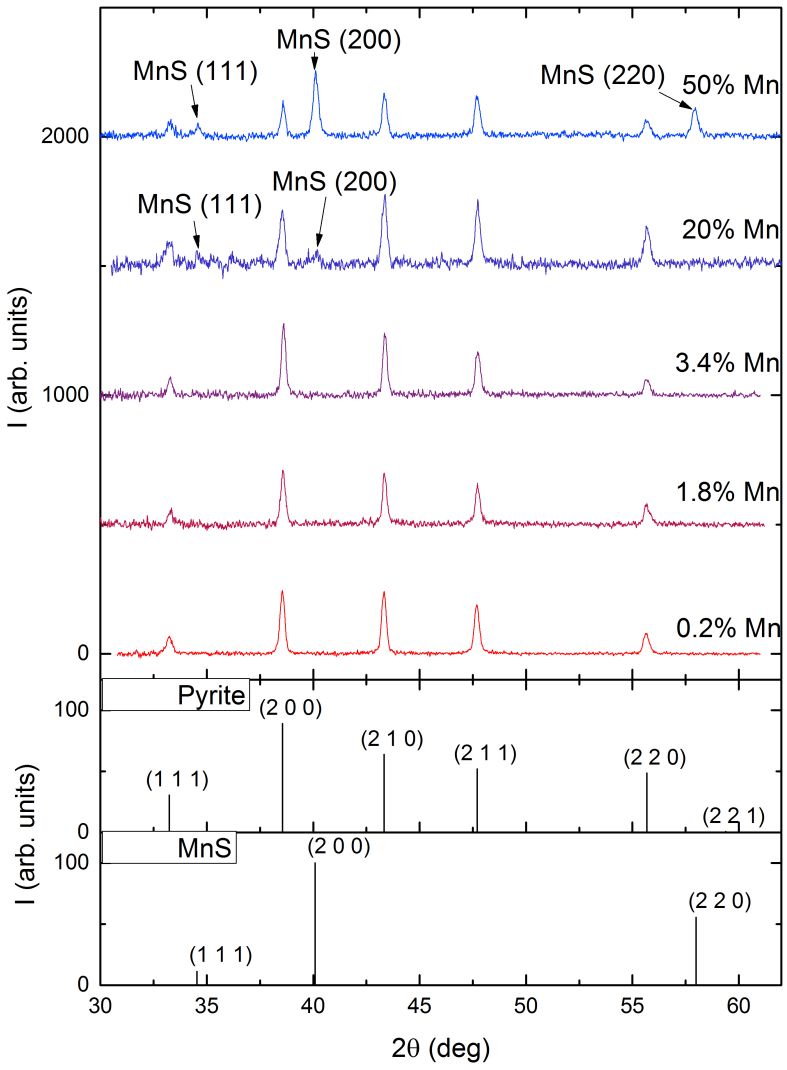

Figure 4.2: XRD patterns as a function of Mn concentration for the sulfidized thin films. All the films were first deposited on $Al_2O_3(0001)$ at 20 $^\circ C$ via D.C. magnetron sputtering and then sulfidized at 600 $^\circ C$. The thickness of these films are 110 nm. 2DXRD was used in these measurements.

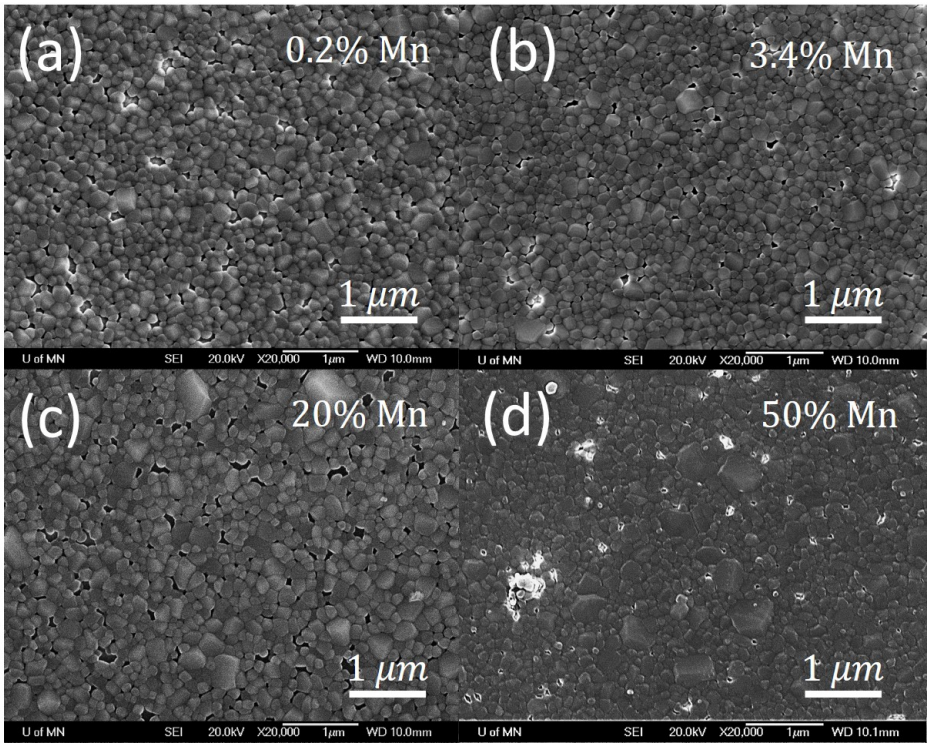

Figure 4.3: SEM images for thin films containing different Mn concentration. The Mn concentration are indicated on the figure.

SEM images for thin films with different Mn concentration are shown in figure 4.3. As shown in this figure, one cannot see any significant structural differences among them, except that there are some large grains shown in the films with high Mn concentrations, (c) and (d). However, the sizes of the grains are still too small to distinguish the chemical composition of the grains with EDS. On the other hand, EDS spectra for high Mn concentration films confirmed that their Mn concentrations were the same as before sulfidation. Thus, there is no Mn lost during the sulfidation.

Unfortunately, MnS is also not detectable by Raman spectroscopy. Consequently,

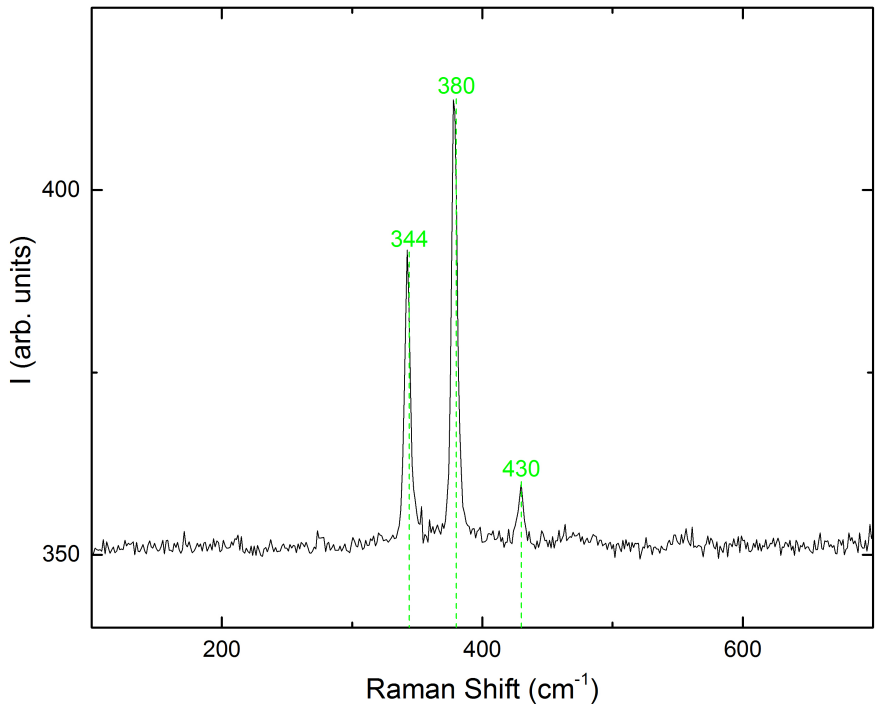

Figure 4.4: Raman spectrum for a representative Mn-doped pyrite thin film with 0.2% Mn.

the Raman spectra of our films look very similar to those for phase pure pyrite FeS_2. For example, figure 4.4 shows a Raman spectrum for a representative Mn-doped pyrite thin film, showing the same peaks as phase pure pyrite FeS_2.

4.2 Electronic Transport Properties

Temperature-dependent resistivity $\rho(T)$ of polycrystalline thin films containing different concentration of Mn was measured across a wide range of temperatures (from

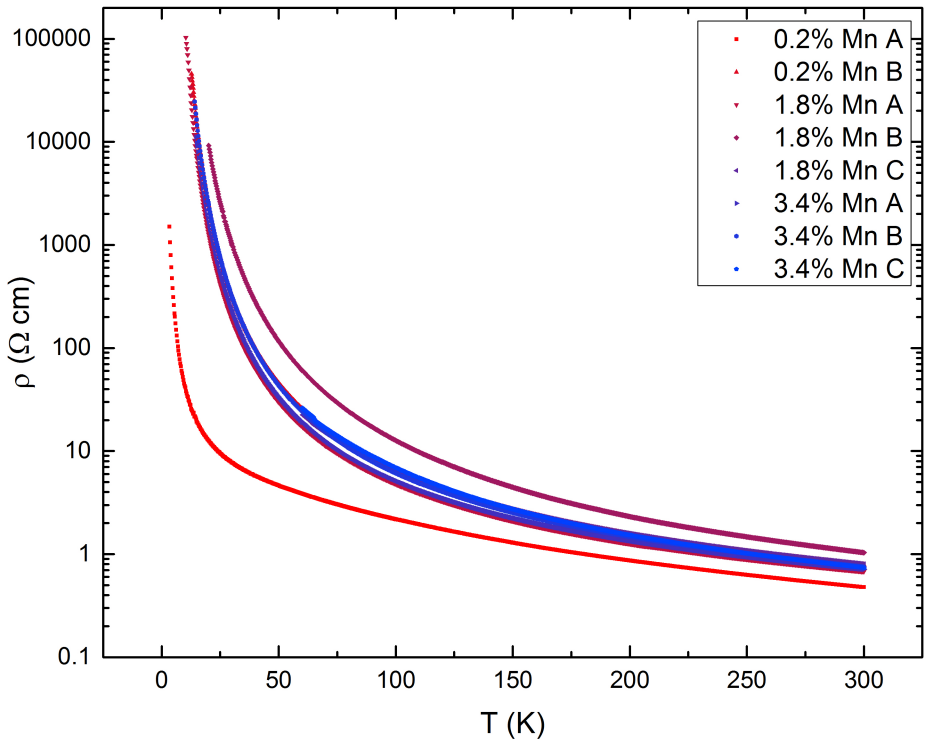

Figure 4.5: Temperature-dependent resistivity for different films. Details for these films were summarized in table 4.1

$\leq 15\ K$ to $300\ K$ for most films). Figure 4.5 shows that the films exhibit semiconductor-like behavior, i.e., $d\rho(T)/dT << 0$. Most films become extremely insulating at low temperatures, the only exception being the film A with 0.2% Mn. These thin films behave very similar to pyrite films that are not intentionally doped with Mn: they exhibit hopping transport, as in our previous research.[7, 8, 31] Table 4.1 summarizes the synthesis conditions and transport properties for the thin films shown in figure 4.5.

According to this table, assuming all dopants were activated, these Mn concentrations should be sufficient to provide a hole carrier concentration from the mid $10^{19}\ cm^{-3}$

Table 4.1: Summary of the synthesis conditions and electronic transport properties for the thin films shown in figure 4.5

Mn (%)	sample	Mn (cm^{-3})	Deposition Temperature	Annealing after Deposition	Sulfidation	$\rho(15K)$ (Ωcm)	$\rho(300K)$ (Ωcm)
0.2	A	5.5×10^{19}	$20°C$	None	$600°C$ $8h$	19.3	0.48
0.2	B	5.5×10^{19}	$20°C$	None	$600°C$ $8h$	1.4×10^{5}	0.79
1.8	A	4.7×10^{20}	$20°C$	None	$600°C$ $8h$	7.3×10^{4}	0.68
1.8	B	4.7×10^{20}	$20°C$	None	$600°C$ $8h$	9.2×10^{4} (at $20K$)	1.03
1.8	C	4.7×10^{20}	$300°C$	$300°C$ $0.5h$	$600°C$ $8h$	N.A.	0.80
3.4	A	8.8×10^{20}	$20°C$	None	$600°C$ $8h$	9.7×10^{4}	0.71
3.4	B	8.8×10^{20}	$20°C$	None	$600°C$ $8h$	9.1×10^{4}	0.75
3.4	C	8.8×10^{20}	$300°C$	$300°C$ $1h$	$600°C$ $8h$	N.A.	0.74

to nearly 10^{21} cm^{-3} range, comparable to the electron carrier concentrations in typical unintentionally doped pyrite thin films.[7] We thus anticipate p-doping if Mn is active. However, these films did not show any indication of p-type conduction in Hall effect measurements, or of decreasing resistivity with increasing Mn concentration. In fact, in most cases the carrier type could not be identified from Hall effect measurements because the Hall signal was suppressed by hopping transport and low mobility of the carriers.[8, 26, 27, 28, 29, 30, 31]

Film A with 0.2% Mn might be the only exception among our films: it exhibits a measurable Hall voltage and Hall resistivity (figure 4.6). This particular film was four orders of magnitude more conductive than others at 15 K and exhibited something close to diffusive transport. Figure 4.6 shows its magnetic field dependent Hall resistivity. Its Hall coefficient R_H is negative and the major carriers are still n-type. The carrier density

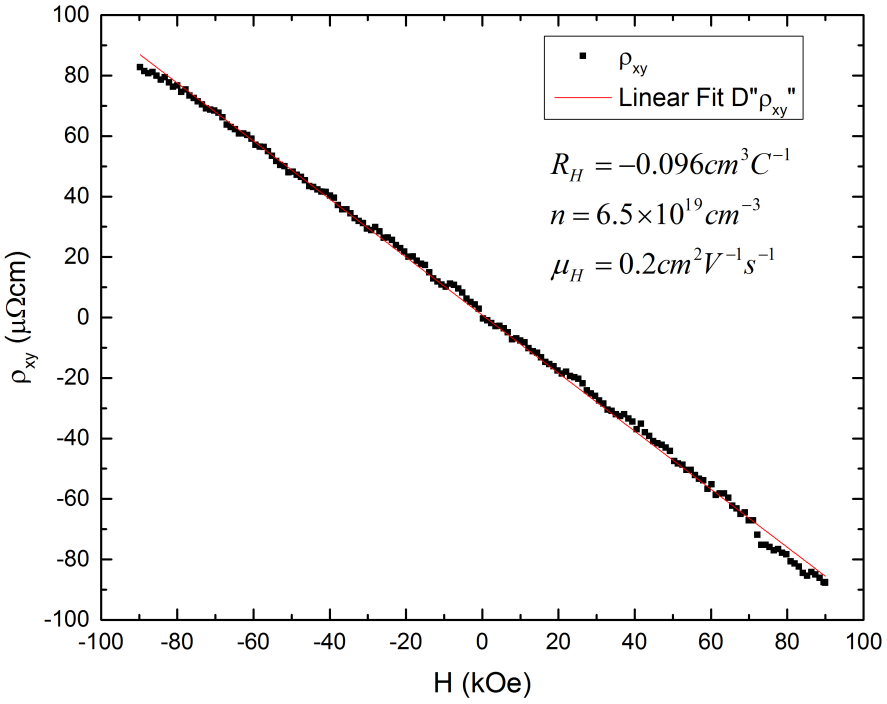

Figure 4.6: Magnetic field dependence of the Hall resistivity ρ_{xy} at 300 K for film A with 0.2% Mn

and the mobility were $n = 6.5 \times 10^{19}\ cm^{-3}$ and $\mu_H = 0.2\ cm^2V^{-1}s^{-1}$, respectively. However, it is just one film, and we have not reproduced this behavior in other films. We thus cannot draw a definitive conclusion on whether the Mn introduced in this film is providing hole carriers.

We investigated the electronic transport mechanism using the temperature dependence of resistivity

$$\rho(T) = \rho_0 \cdot exp(\frac{T_0}{T})^{-m} \tag{4.1}$$

where $\rho_0 = \rho(T \to \infty)$ and T_0 is a characteristic temperature. For conventional diffusive

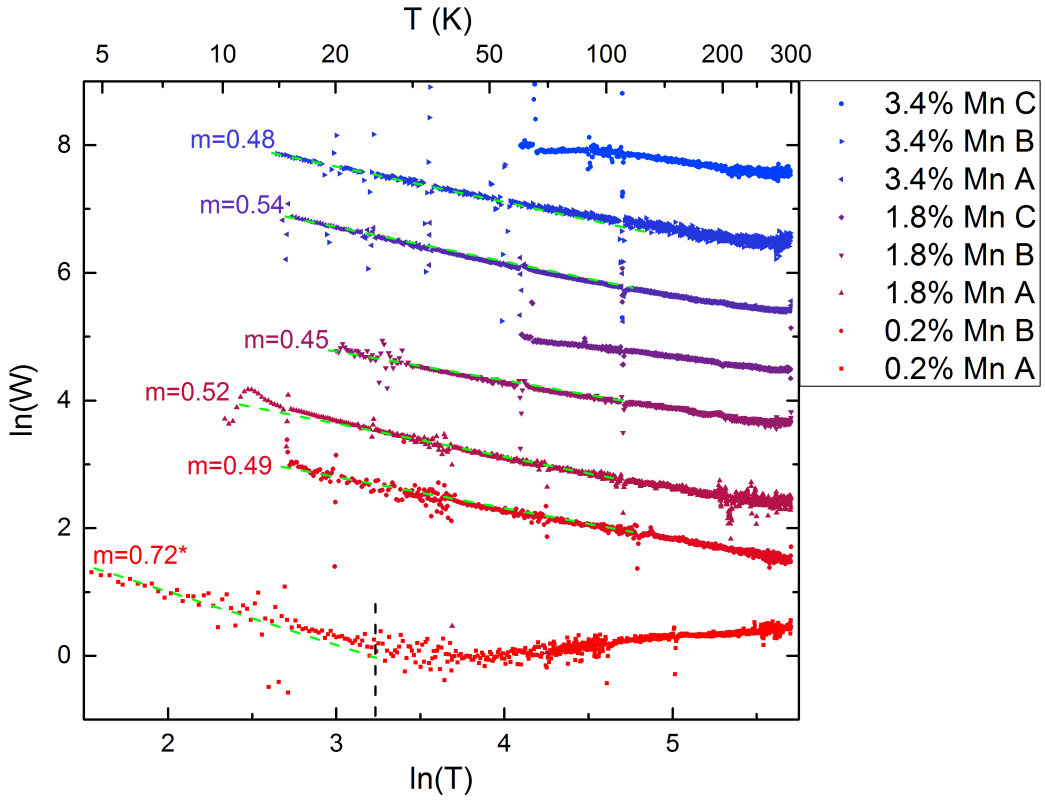

Figure 4.7: $ln(W)$ vs. $ln(T)$ plots for films listed in table 4.1. *: m for film A with 0.2% Mn was obtained only from the left part of the black dashed line.

semiconductor transport $m \approx 1$, while for hopping transport $m \approx 1/2$. To extract the value of m, we plotted $ln(W)$ vs. $ln(T)$, where $W = -d(ln(\rho))/d(ln(T))$. The slope of this plot is $-m$. Figure 4.7 shows the $ln(W)$ vs. $ln(T)$ plot for the films in figure 4.5. All the films except the film A with 0.2% Mn show a $\rho = \rho_0 exp(T_0/T)^{-1/2}$ relationship in the measured temperature range up to 300 K, a clear sign of hopping transport.

Zhang et al. showed that unintentionally doped pyrite thin films exhibit hopping

transport due to metallic Fe, or metallic FeS impurities in pyrite FeS_2.[7, 8] Our Mn-doped films behave similarly, and we propose that hopping is due to similar inhomogeneities. We propose three possibilities for our films in figure 4.8. The first possibility is that there may be insulating MnS on the grain boundaries, as shown figure 4.8 (a). A second possibility is that there are randomly distributed MnS impurities in our FeS_2, as shown in figure 4.8 (b). Finally, the films may simply be electronically inhomogeneous, as shown in figure 4.8 (c).

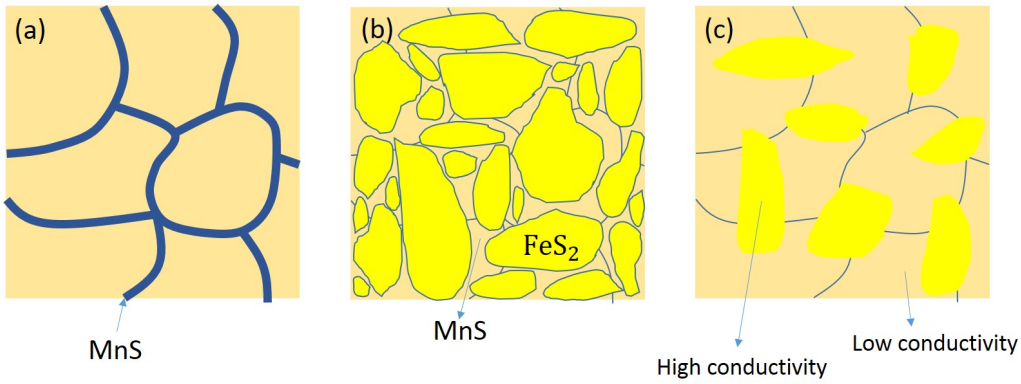

Figure 4.8: Possible inhomogeneities in our Mn-doped thin films. (a) There are insulating MnS on the grain boundaries. (b) FeS_2 and MnS are distributed randomly. (c) They may be electronically inhomogeneous.

Regardless of the exact situation, we conclude hopping transport arising due to local variations in conductivity on a nanoscopic scale. This is a general problem with FeS_2 films synthesized in this way. Finding a way to avoid it would allow us to better probe whether Mn doping is really effective for p-type generation.

Chapter 5

Conclusion and Discussion

Pyrite FeS_2 has long been recognized as a good candidate for solar cells. However, its performance has been limited by some unknown reasons. One of the reasons for the lack of progress is the presence of unknown and unintentional dopants. Identifying these unknown dopants remains a big challenge, as does controlled n- and p-type doping. Given that unintentionally doped pyrite films are n-type, we provide an approach to study doping by intentionally introducing Mn into pyrite FeS_2 thin films, which we may produce a p-type pyrite thin film. Development of a p-type dopant would therefore enable p-n junctions, a key step in creating a pyrite based solar absorber.

In chapter 3, we studied the chemical and structural properties of the $Fe_{1-x}Mn_x$ thin films before sulfidation. We found that they were in an unexpected metastable bcc solid solution of Fe-Mn. At temperatures higher than about 400 $^{\circ}C$, a phase transformation occurs and they become mixed-phases of bcc and fcc phases.

In chapter 4, we studied the chemical, structural and electronic transport properties of the Mn-doped pyrite thin films. A secondary phase of MnS was detected via XRD in high Mn concentration films ($> 20\%$). Though in low Mn concentration films ($< 5\%$) this secondary phase was not detected via XRD, the electronic transport properties of the films with low Mn concentration indicate that there were nanoscale inhomogeneities originating from *ex situ* sulfidation, which lead to hopping transport in these films. Finally, we found that the resulting Mn-doped pyrite films were not p-type.

In future studies, we would suggest a two-step sulfidation for Mn-doped films: (1) sulfidation at a low temperature between 200 $^{\circ}C$ and 400 $^{\circ}C$; followed by (2) further annealing in sulfur vapor at 600 $^{\circ}C$ after all bcc metastable phase converts. In addition, we would also suggest introducing Mn into pyrite single crystals, whose native dopant levels can be five orders of magnitude lower than pyrite films. Other p-type dopants such as P, As are also worth trying in both thin films and single crystals.

References

[1] A. Ennaoui, S. Fiechter, C. Pettenkofer, N. Alonso-Vante, K. Bker, M. Bronold, C. Hpfner, H. Tributsch, Sol. Energy Mater. Sol. Cells 29 (1993) 289- 370.

[2] K. Momma, F. Izumi, J. Appl. Cryst. 44 (2011) 1272-1276.

[3] M. Cabn-Acevedo, M.S. Faber, Y. Tan, R.J. Hamers, S. Jin, Nano Lett. 12 (2012) 1977- 1982.

[4] N. Berry, M. Cheng, C.L. Perkins, M. Limpinsel, J.C. Hemminger, M. Law, Adv. Energy Mater. 2 (2012) 1124-1135.

[5] Y. Bi, Y. Yuan, C.L. Exstrom, S.A. Darveau, J. Huang, Nano Lett. 11 (2011) 4953-4957.

[6] S. Seefeld, M. Limpinsel, Y. Liu, N. Farhi, A. Weber, Y. Zhang, N. Berry, Y.J. Kwon, C.L. Perkins, J.C. Hemminger, R. Wu, M. Law, J. Am. Chem. Soc. 135 (2013) 4412- 4424.

[7] X. Zhang, Ph.D. thesis, University of Minnesota (2015).

[8] X. Zhang, M. Manno, A. Baruth, M. Johnson, E. S. Aydil and C. Leighton, ACS Nano 7 (2013) 2781- 2789.

[9] Arthur W. Sleight, Tom A. Bither, Inorg. Chem., 8,3 (1969) 566- 569.

[10] S. W. Lehner, N. Newman, M. van Schilfgaarde, S. Bandyopadhyay, K. Savage, and P. R. Buseck, J. Appl. Phys. 111, 083717 (2012).

[11] K. Adachi, K. Sato, S. Kubo, and K. Yamauchi, J. Phys. Soc. Japan 30 (1971) 577.

[12] Q. Yu, S. Cai , Z. Jin, Z. Yan, Materials Research Bulletin 48 (2013) 3601- 3606.

[13] Miguel Cabn-Acevedo, Michael L. Stone, J. R. Schmidt, Joseph G. Thomas, Qi Ding, Hung-Chih Chang, Meng-Lin Tsai, Jr-Hau He, and Song Jin, Nature Materials 14 (2015) 1245- 1251.

[14] W. H. Bragg, W. L. Bragg, Proc R. Soc. Lond. A. 88, 605 (1913) 428.

[15] U. Pietsch, V. Hol, and T. Baumbach, High-Resolution X-Ray Scattering: From Thin Films to Lateral Nanostructures (Springer, New York, 2004).

[16] L. J. van der Pauw, Philips Res. Rep. 13 (1958) 1.

[17] C. Kittel, Introduction to Solid State Physics (John Wiley & Sons, New York, 2005).

[18] http://resource.npl.co.uk/mtdata/phdiagrams/femn.htm

[19] J. Saha, B. Bolon, A. Abin-Fuentes, J.S. Parker, C. Leighton and R. Victora, J. Appl. Phys. 102, 073901 (2007).

[20] B.D. Cullity, S.R. Stock, Elements of X-Ray Diffraction, 3rd Ed., Prentice-Hall Inc., 2001, 167-171

[21] L. Vegard, Zeitschrift fr Physik. 5, 1 (1921) 17- 26.

[22] K. Sumiyama, M. Kadono and Y. Nakamura, Transactions of the Japan Institute of Metals, 22, 10 (1981) 686- 690.

[23] K. Sumiyama andY. Nakamura, Transactions of the Japan Institute of Metals, 23, 10 (1982) 595- 598.

[24] K. Sumiyama andY. Nakamura, Journal of Magnetism and Magnetic Materials 35 (1983) 219- 220.

[25] B.I. Shklovskii, A.L. Efros, Electronic Properties of Doped Semiconductors, Springer-Verlag, Berlin; New York, 1984.

[26] P. Sheng, B. Abeles, Y. Arie, Phys. Rev. Lett. 31 (1973) 44- 47.

[27] B. Abeles, P. Sheng, M.D. Coutts, Y. Arie, Adv. Phys. 24 (1975) 407- 461.

[28] M. Pollak, C.J. Adkins, Philos. Mag. Part B 65 (1992) 855- 860.

[29] J. Zhang, B.I. Shklovskii, Phys. Rev. B 70 (2004) 115317.

[30] I.S. Beloborodov, A.V. Lopatin, V.M. Vinokur, K.B. Efetov, Rev. Mod. Phys. 79 (2007) 469- 518.

[31] X. Zhang, T. Scott, T. Socha, D. Nielsen, M. Manno, M. Johnson, Y. Yan, Y. Losovyj, P. Dowben, E.S. Aydil, C. Leighton, ACS Appl. Mater. Interfaces 7 (2015) 14130- 14139.

[32] R.J. Kennedy, P.A. Stampe, E. Hu, P. Xiong, S. von Molnr, Y. Xin, Appl. Phys. Lett. 84 (2004) 2832- 2834.